J. Fluid Mech. (2007), *vol.* 589, *pp.* 261–303. © 2007 Cambridge University Press
doi:10.1017/S0022112007007720 Printed in the United Kingdom

Turbulent wake of an inclined cylinder with water running

MD. MAHBUB ALAM AND Y. ZHOU†
Department of Mechanical Engineering, The Hong Kong Polytechnic University, Hung Hom, Kowloon, Hong Kong

(Received 10 August 2006 and in revised form 21 May 2007)

This paper presents the results of an experimental study of fluid dynamics around an inclined circular cylinder with and without water running over its surface, covering water rivulet formation, fluid forces on the cylinder, near wake and their interrelationships. The cylinder inclination angle (α) with respect to incident flow was between 55° and 80°. It has been found that water running over the cylinder surface may behave quite differently, depending on the Reynolds number (*Re*), and subsequently impact greatly upon the fluid dynamics around the cylinder. As such, five flow categories are classified. Category *A*: one water rivulet was observed, irrespective of α, at the leading stagnation point at a small *Re*. Category *B*: the rivulet splits into two, symmetrically arranged about the leading stagnation line, once *Re* exceeds a critical value that depends on α. The two rivulets may further switch back to one, and vice versa. Category *C*: two symmetrical straight rivulets occur. Category *D*: the two rivulets shift towards the flow separation line with increasing *Re* and oscillate circumferentially. The oscillation reaches significant amplitude when the rivulets occur at about 70° from the leading stagnation point. This increased amplitude is coupled with a rapid climb in the mean and fluctuating drag and lift, by a factor of near 5 for the fluctuating lift at $\alpha = 80°$. Meanwhile, the flow structure exhibits a marked variation. For example, Strouhal number and vortex formation length decrease, along with an increase in spanwise vorticity concentration, velocity deficit, and coherence between vortex shedding and fluctuating lift. All these observations point to the occurrence of a 'lock-in' phenomenon, i.e. the rivulet oscillation synchronizing with flow separation. A rivulet–vortex-induced instability is proposed to be responsible for the well reported rain–wind-induced vibration associated with the stay cables of cable-stayed bridges. Category *E*: the two rivulets shift further downstream just beyond the separation line; the shear layers behind the rivulets become highly turbulent, resulting in weakened vortex shedding, flow fluctuating velocities and fluctuating fluid forces. Based on the equilibrium of water rivulet weight, aerodynamic pressure and friction force between fluid and surface, an analysis is developed to predict the rivulet position on the cylinder, which agrees well with measurements.

1. Introduction

Cables are the most important component of cable-stayed bridges and are susceptible to violent vibrations under light-to-moderate wind and rain. Simultaneous presence of rain and wind results in two running water rivulets along the cables,

---

† Author to whom correspondence should be addressed: mmyzhou@polyu.edu.hk.

which are the main cause of the so-called rain–wind-induced (RWI) cable vibration. This vibration may have peak-to-peak amplitude up to six times the cable diameter, thus reducing the fatigue life of the cable, and even causing cable damages (e.g. Verwiebe & Ruscheweyh 1998) and jeopardizing the safety of the entire bridge. The cost associated with a typical failure can easily amount to millions of dollars. As such, it is not surprising that extensive efforts have been made to investigate the mechanisms of the RWI vibration.

Investigations of the RWI vibrations have so far included field measurements, wind tunnel tests, theoretical and numerical analyses. Water rivulets, formed under the natural rain–wind conditions, are not easy to model in wind tunnels. Four approaches have been reported to simulate rivulets on a cable model (i) spray water shower onto the cable model to form rivulets in a wind tunnel (Hikami & Shiraishi 1988; Flamand 1995; Matsumoto *et al.* 1995; Verwiebe & Ruscheweyh 1998); (ii) release water at the upper end of the cable model in a wind tunnel (Wang *et al.* 2005); (iii) fix artificial stationary rivulets on the cable surface, used in both wind tunnel tests and numerical analysis (e.g. Yamaguchi 1990; Gu & Lu 2001); (iv) create artificial rivulets oscillating at the same frequency of a vibrating cable, which was used in numerical analysis (Cao, Tucker & Wang 2003; Wilde & Witkowski 2003; Xu & Wang 2003; Burton *et al.* 2005) and also experimental investigations (Matsumoto *et al.* 2005*a*).

The RWI vibration occurs for a limited range of wind speeds and often at a yaw angle of 20°–60°; it is always associated with water rivulets running along the cable and oscillating circumferentially (Yoshimura *et al.* 1988; Flamand 1995). In general, two water rivulets are observed, one on the lower windward side of the cable and the other on the upper leeward side. While the former plays a negligible role, the latter is largely responsible for the RWI vibration (Ohshima 1987; Hikami & Shiraishi 1988; Flamand 1995; Bosdogianni & Oliveri 1996). It is now established that the RWI vibration, characterized by a much lower frequency but much larger amplitude, is not a simple vortex-induced oscillation. The wake galloping is also excluded because the cables in engineering are separated sufficiently far to avoid any interactions between them (Hikami & Shiraishi 1988). Matsumoto *et al.* (1995) advocated three types of RWI cable vibration, namely, the 'galloping' type caused by the rivulets and/or axial flow, the vortex-shedding type with a longer period than the classical Kármán vortex shedding, and a combination of both. Flamand (1995) conducted full-scale wind tunnel tests and observed the RWI cable vibration. However, once replacing the moving water rivulets by false fixed rivulets glued on the cable surface, he failed to reproduce the RWI vibration. He concluded that the oscillation of the upper water rivulet played a crucial role in the generation of the RWI vibration. This opinion was shared by Verwiebe & Ruscheweyh (1998) who suggested that the oscillation of water rivulets resulted in a variation in the cable cross-section shape and hence in the pressure distribution around the cable. The resultant force on the cable varied and subsequently excited the cable. Cosentino, Flamand & Ceccoli (2003*a*) performed extensive wind tunnel measurements, including unsteady pressure field, rivulet thickness and circumferential movement around a cable model under excited conditions. Their data indicated that the rivulets oscillated at half the cable oscillation frequency, which was inconsistent with Yamaguchi's (1990) suggestion that the upper rivulet oscillation synchronized with the cable vibration. They subsequently proposed that the RWI vibration was due to the oscillation of the upper rivulet, which caused a change in the flow pattern from that at the subcritical Renolds number to that at the critical Reynolds number (single-bubble flow regime). Once reaching the farthest position from the leading stagnation point, the upper rivulet gained its maximum thickness and the shear layer separating from this rivulet reattached behind the rivulet, resulting in a single bubble on the cylinder surface. On the other hand, when the upper rivulet was at the position nearest to the leading stagnation point, the rivulet thickness was minimum, and the shear layer separating from the rivulet would not reattach on the cylinder surface, leading to a flow pattern similar to that around a clean cylinder at a subcritical Reynolds number. Wang *et al.* (2005) investigated experimentally the formation process of water rivulets along an inclined cable and their effects on the near wake. They observed the circumferential oscillation of water rivulets, which was associated with a substantial increase in drag, and proposed that the circumferential oscillation of the water rivulets could possibly be synchronized with flow separation.

Previous work has greatly improved our understanding of the RWI vibration, and has guided the development of a number of techniques in bridge engineering to alleviate the problem, for example, increasing damping by using damping ropes between the cables, dynamic vibration absorbers, and dashpots at the cable footing, deflecting water on the cable surface or preventing water rivulets from oscillating circumferentially. These techniques, though effective, are not enough to eradicate the problem, probably because a thorough understanding of the RWI vibration has yet to be developed, including its generation mechanisms (Matsumoto *et al.* 2001). Most previous investigations focused on engineering issues such as how, when and where the problem occurred. There does not seem to have been a systematic study of the fluid dynamics associated with this problem in spite of the fact that the RWI vibration originates from fluid excitation forces; many important issues remain to be clarified. For example, the RWI excitation forces on a cable, though crucial in understanding the RWI cable vibration, are neither well documented nor understood. Questions remain to be answered on how the rivulets depend on the wind speed, and how their occurrence affects the near wake, dominant frequency and flow three-dimensionality.

This work aims to conduct a comprehensive study of fluid dynamics associated with an inclined stationary cable with and without running water rivulets, and to develop our understanding of the effects of running water rivulets on the near-wake fluid dynamics, covering the formation and characteristics of water rivulets, and their connection to the fluid forces and the near wake. Experimental details are given in § 2, the water rivulet formation and dependence on the wind speed is presented in § 3, fluid forces are examined in § 4 and the near wake is characterized in § 5. One possible mechanism of the RWI vibration is proposed in § 6, and conclusions are drawn in § 7.

2. Experimental details

2.1. *Experimental set-up*

Experiments were performed in a low-speed open-circuit wind tunnel with a 1 m long square test section of 0.3 m × 0.3 m. The walls of the test section were made of Perspex to facilitate the observation of water rivulets. The free-stream velocity (U_∞) investigated was increased from 0 to 15 m s^{-1}, corresponding to an *Re* (based on U_∞ and the cable diameter d) of $0 \sim 22\,000$, covering the wind speed at which the RWI vibration occurs (e.g. Gu & Du 2005). The wind speed was measured using a standard Pitot-static tube connected to an electronic micro-manometer (Furness Control, model FCO510). At this *Re* range, the maximum longitudinal turbulent intensity was 0.7 % in the free stream, and the velocity was uniform to within 1.5 %. The laboratory was air-conditioned, with the temperature maintained at 25°C.

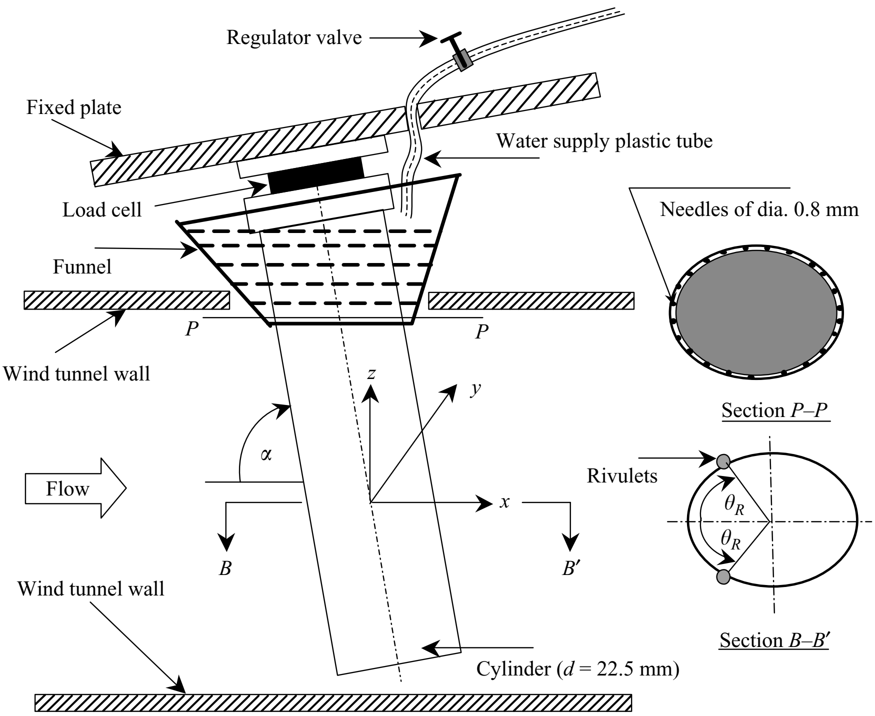

FIGURE 1. Experimental set-up.

The cable was modelled by a cantilevered circular brass tube (figure 1), mounted across the working section in a vertical plane at the mid section, 0.2 m downstream from the exit plane of the contraction, that is, the yaw angle (β) of the cylinder was zero. Although many previous investigations were made with the cylinder both yawed and inclined, the RWI vibration was observed for the cylinders of $\beta = 0$ (Zasso, Bocciolone & Brownjohn 1992; Matsumoto *et al.* 1995). Investigation in the case of $\beta = 0$ is relatively simple. Nevertheless, the physics and mechanisms of the RWI vibration unravelled for $\beta = 0$ should be also valid for $\beta \neq 0$.

The RWI vibration of a stay cable could occur at any α, including nearly vertical cables such as those near the girders (Ruscheweyh & Verwiebe 1995; Verwiebe & Ruscheweyh 1998), though most of engineering observations were made at $\alpha \neq 0$ (Ruscheweyh & Verwiebe 1995; Verwiebe & Ruscheweyh 1998; Gu & Du 2005). The present work aims to understand the associated fluid dynamics or the generation mechanism behind the RWI vibration, which is expected to be the same for different α values. As such, it is reasonable for the investigation to be conducted at a given α. In general, a larger α corresponds to a smaller *Re*, at which the RWI vibration occurs (Gu & Du 2005). Systematic measurements were performed for $\alpha = 90°$, 80° and 55°, where $\alpha = 55°$ is close to the cases examined by others (e.g. Cheng & Tanaka 2005; Gu & Du 2005) and $\alpha = 80°$ is chosen to examine the possible dependence on α of water rivulets and other aspects of the RWI vibration.

The tube outer diameter d was 22.5 mm, causing a blockage of about 7.5 %, and a minimum aspect ratio of 13.3. No end plates were mounted on the cylinder. The lower end of the cylinder, sealed with a flat brass cap, had a clearance of about 2–3 mm from the bottom wall of the working section. Note that, at $\alpha = 55°$, the cylinder length was adjusted so that nearly the same clearance (2–3 mm) was maintained. Tests were conducted by varying the clearance from 1 to 6 mm; there were no appreciable changes in time-averaged and fluctuating forces on the cylinder, probably because the end was within the low-speed wall boundary layer, whose thickness was estimated to be about 15 mm at $U_\infty = 8\,\mathrm{m\,s^{-1}}$.

Water was released, through a funnel with an inner diameter of 24.1 mm, uniformly at the upper end of the cylinder at a rate of $Q = 25$ and $30\,\mathrm{l\,h^{-1}}$ (figure 1). Unless otherwise stated, the data at $Q = 25\,\mathrm{l\,h^{-1}}$ is presented in this paper. The water flow rate, adjustable by a regulator valve, was made steady by maintaining a constant water level in a water tank placed at about 2.25 m above the test section. In order to make sure of a uniform gap around the cylinder between the cylinder surface and the funnel, eighteen 0.8 mm diameter needles were placed with equal spacing in the gap. The angle θ_R denotes the position of rivulets, measured from the leading stagnation line. The formation and characteristics of the water rivulets were recorded using a digital video camera (Sony DCR-PC100E).

2.2. *Important dimensionless parameters*

$Re = \rho_a U_\infty d / \mu_a$ (ρ_a and μ_a are the density and viscosity of air, respectively) is a relevant dimensionless parameter even for inclined cylinders (e.g. King 1977; Ramberg 1983; Hayashi & Kawamura 1995; Cheng & Tanaka 2005). Other dimensionless parameters include force coefficients ($= Force/0.5\rho_a U_\infty^2 \times Area$), Strouhal number, $St (= f_s d/U_\infty$, where f_s is the vortex shedding frequency), and parameters such as x^*, y^*, z^* and rivulet thickness h^* which characterize the rivulet shape. In this paper, an asterisk denotes normalization by d and/or U_∞. The size of the rivulet varies little with U_∞, but significantly with water flow rate Q. Therefore, Q is given in terms of the Reynolds number of water flow ($Re_w = \rho_w (Q/A_r) h/\mu_w$, where ρ_w and μ_w are the density and viscosity of water, respectively, and A_r is the cross-sectional area of the rivulet) along the cylinder.

2.3. *Force measurements*

Forces on the cylinder were measured using a three-component quartz piezoelectric load cell (Kistler Model 9251A) characterized by high response, resolution and stiffness. The load cell mounted on the top end of the cylinder was bolted tightly between two machine-polished stainless steel blocks (figure 1). In order to avoid the effect of wind tunnel vibration on measurements, the holder of the load cell was mounted on an external rigid frame detached from the wind tunnel. The load cell measures instantaneous integral fluid forces acting on the length of the cylinder exposed within the wind tunnel. The preload of the load cell was 25 kN, exceeding 7.4×10^4 times the forces measured at present, resulting in a very high signal-to-noise ratio in the measurement of fluid forces. Static calibrations of the load cell in the lift and drag directions were carried out using dead weights. The load cell had a high linearity in the load/output relation.

2.4. *PIV measurements*

A Dantec particle image velocimetry (PIV) system (Xu, Zhou & Wang 2006), was used to measure the near wake of the cylinder in the (x, y)-plane. The flow was seeded by smoke, generated from paraffin oil, with a particle size of about 1 μm in diameter. Each image from PIV measurements covered an area of $x^* = 0.7$–6.6 (130 mm) and $y^* = -2.4$–2.4 (104 mm) for $\alpha = 80°$ and $x^* = 1$– 6.7 (128 mm) and $y^* = -2.25$–2.25 (101 mm) for $\alpha = 55°$. The origin of the coordinate system is defined at the center of the cylinder; the x-axis is along U_∞, the y-axis is perpendicular to the x-axis in the horizontal plane and the z-axis is normal to both x and y, following the right-hand system (figure 1). In image processing, an interrogation window of 64×64 pixels (approximately $6.5\,\text{mm} \times 6.5\,\text{mm}$, or $0.29d \times 0.29d$) was used with 50 % overlap in each direction. The ensuing in-plane velocity field consisted of 40×32 vectors, which produced the same number of vorticity data points. The spatial resolution for vorticity data was about $0.15d$.

2.5. *LDA measurements*

A two-component LDA (Dantec Model 58N40 LDA with enhanced FVA signal processor) was used to measure the cross-flow distributions of time-averaged and root mean square (r.m.s.) velocities at $x^* = 1$, 1.5, 2 and 3 over $y^* = -4 \sim 4$. This measurement was conducted in a different wind tunnel, whose test section was 0.6 m in width, 0.6 m in height and 2.4 m in length. See Zhou, Zhang & Yiu (2002) and Huang, Zhou & Zhou (2006) for more details of this tunnel. The test model has the same diameter as used in measurements introduced in §§ 2.1, 2.2 and 2.3. The LDA system was mounted on a three-dimensional computer-controlled traversing mechanism, with a traversing resolution of 1 μm. The lateral increment, Δy^*, in LDA measurements was 0.09 for $y^* = -2$–2 and 0.18 for $y^* = -4$– −2 and 2–4. The LDA measuring volume has a minor axis of 1.18 mm and a major axis of 2.48 mm. The flow seeding was the same as used in PIV measurements.

2.6. *Hotwire measurements*

A single tungsten wire of 5 μm in diameter, operated at an overheating ratio of 1.8 on a constant temperature circuit, was placed at $x^* = 4$, $y^* = 1.5$ to measure the predominant frequency in the wake. The hot-wire signal was offset, amplified and then digitized using a 12-bit A/D board at a sampling frequency of 1.0 kHz. The duration of each hot-wire signal was about 16.2 s.

In order to check the spanwise uniformity of the flow on the cylinder, we measured the vortex-shedding frequency ($\alpha = 90^\circ$) at $z^* = 04$, ± 3 and ± 5.5 and observed no change, suggesting a negligible end effect. Hayashi & Kawamura (1995) measured peripheral surface-pressure distribution over $z^* = -10$–10 ($\Delta z^* \cong 0.5$) of an inclined cylinder ($\alpha = 60^\circ$) with a length-to-diameter ratio of 20. They observed the same pressure distributions for $z^* = -8$–10, and only a slight deviation in the base pressure for the remaining z^*. Note that $z^* = -10$ corresponds to the upstream end. The length-to-diameter ratio of the present cylinder was 17 at $\alpha = 55^\circ$, close to the value of 20 used by Hayashi & Kawamura. Therefore, the *St*, LDA and PIV measurements were conducted only at $z^* = 0$ and are expected to be the same in other planes parallel to $z^* = 0$.

3. Formation of water rivulets

At $\alpha = 90^\circ$ and $Re = 0$ ($U_\infty = 0$), water through the gap between the funnel and the cylinder surface flows uniformly around the cylinder, forming a water film. At $\alpha \neq 90^\circ$ and $Re = 0$, water moves towards the leading or trailing stagnation line, immediately after passing through the gap, owing to the gravity, and then flows along the line. Figure 2 presents the typical photographs of the cylinder, with water running, inclined at $\alpha = 80^\circ$ and 55°, respectively. In general, for very small *Re*, the wind force is insufficient to split water flow, and water through the gap between the funnel and the cylinder surface forms only a single water rivulet along the leading stagnation line, similarly to the case of $Re = 0$ (figure 2*a*). The water rivulet splits into two once *Re* exceeds a level, which depends on α. The rivulets occur almost symmetrically about

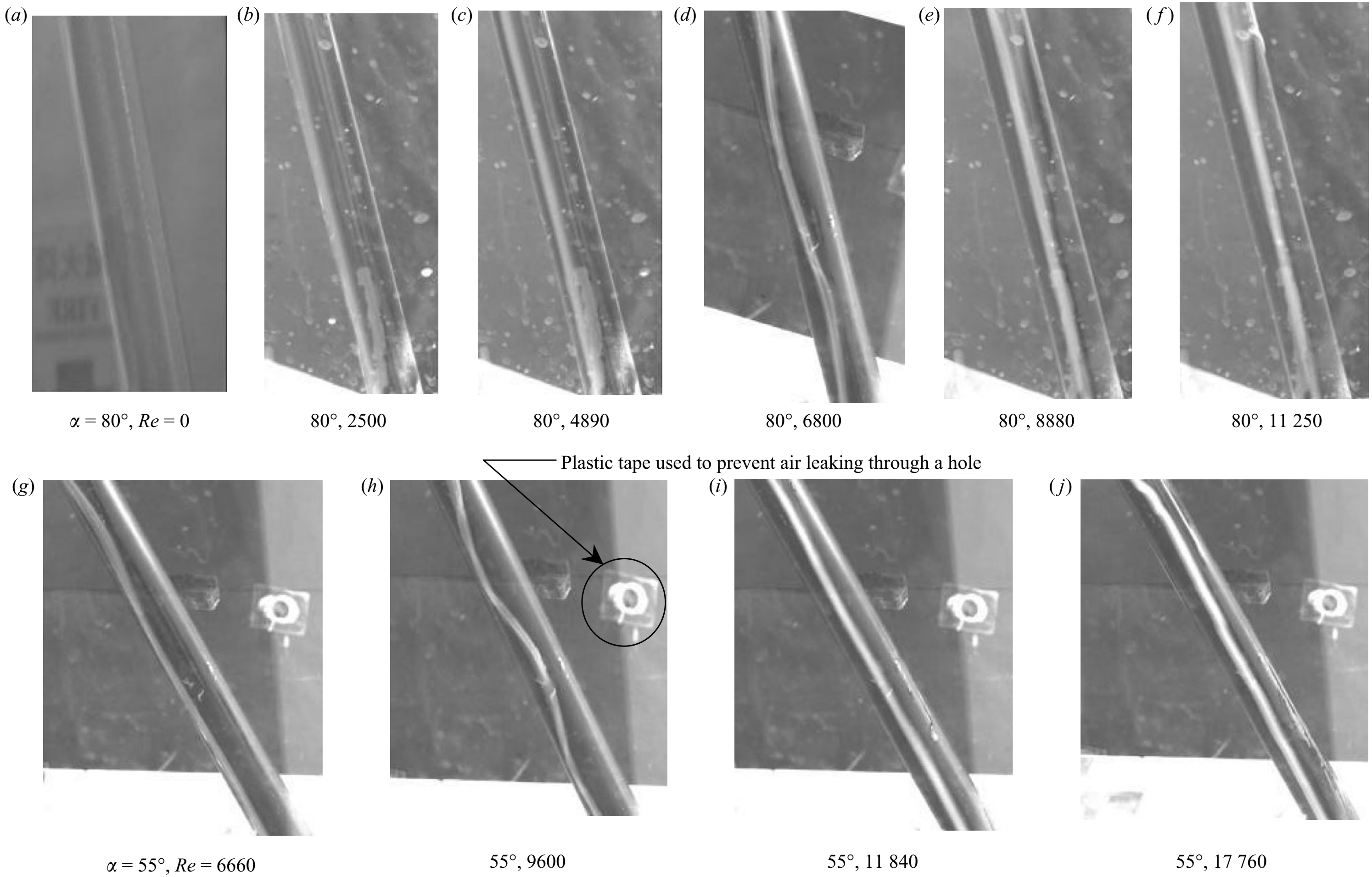

FIGURE 2. Photographs of running water rivulets. Flow is left to right.

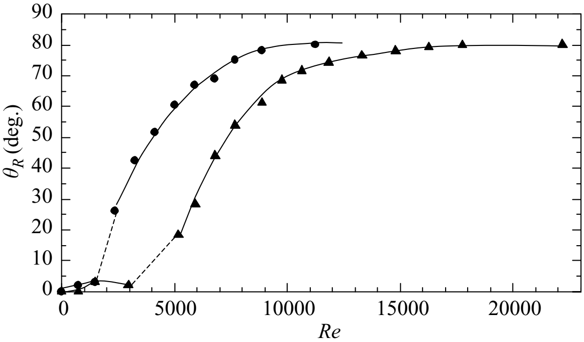

FIGURE 3. Dependence of water rivulet position (θ_R) on *Re*. Dashed line indicates the transition from one to two rivulets, where one and two rivulets may occur intermittently. ●, $\alpha = 80°$; ▲, $\alpha = 55°$.

the stagnation lines. For a further increase in *Re*, the rivulets shift towards the flow separation lines.

The rivulets appear quite straight along the cylinder for relatively low and high *Re* (figure 2*b*, *c*, *e*, *f*, *g*, *i*, *j*), but become sinusoidal, oscillating circumferentially, at an intermediate *Re*, about 6800 for $\alpha = 80°$ (figure 2*d*) and 9600 for $\alpha = 55°$ (figure 2*h*). The axial wavelength of the sinusoidal rivulets is estimated to be about 5*d* at $\alpha = 80°$ and 3.5*d* at $\alpha = 55°$, larger than Wang *et al.*'s (2005) observation (2*d*) at $\alpha = 45°$ and $\beta = 45°$. This is reasonable; a larger α should correspond to a longer wavelength because of the enhanced two-dimensionality of the near wake at a large α (Ramberg 1983). A difference in β and the water flow rate, $8\ \mathrm{l\,h^{-1}}$ by Wang *et al.* and $25\ \mathrm{l\,h^{-1}}$ at present, should also contribute to the deviation between the present and Wang *et al.*'s results.

The photographs indicate that the width of the rivulet is almost constant along the cylinder axis for relatively low velocities but varies when the rivulets oscillate, which is particularly noticeable at $Re = 6800$ for $\alpha = 80°$ and $Re = 9600$ for $\alpha = 55°$ (figure 2*d*, *h*). The thickness and width of a rivulet on the cylinder surface were estimated from photographs taken at 0° and 90°, respectively, with respect to the cylinder diameter through this rivulet. They are about 2.76 mm and 3.3 mm, respectively, for $Re = 6800$ and $\alpha = 80°$, and 2.97 mm and 3.06 mm, respectively, for $Re = 9600$ and $\alpha = 55°$. The resulting h^* is 0.12 ($Re_w = 31$) and 0.13 ($Re_w = 34$) for $\alpha = 80°$ and 55°, respectively, corresponding to a Bond number of $B_o = \rho_w g d^3/8h\sigma$ (Reisfeld & Bankoff 1992; Oron, Davis & Bankoff 1997; Lemaitre *et al.* 2006) = 68 and 53, respectively, where σ is the surface tension of water. The B_o range implies that the surface tension force is negligible compared to the inertial/gravitational force, and the rivulet maintains a constant cross-section. This information serves merely to provide a rough dimension of the rivulet, which shows little dependence on *Re*.

Figure 3 presents the dependence on *Re* of θ_R, estimated from photographs. At $\alpha = 80°$, θ_R is about zero (one rivulet only) at $Re < 1500$ but jumps abruptly to 28° (two rivulets) at $Re = 2500$, and continues its rise for further increasing *Re*. As *Re* exceeds 8400, θ_R is about 81° and remains unchanged for further increasing *Re*. At $\alpha = 55°$ a single rivulet is formed near the leading stagnation line for $Re < 3000$ (figure 3). At $Re = 5200$, which is higher than the critical *Re* (2500) at $\alpha = 80°$, this rivulet splits into two, with θ_R jumping to 16.5°. The difference in the critical *Re* between $\alpha = 80°$ and 55° depends on the tangential component of rivulet weight. A smaller α corresponds to a larger tangential component of rivulet weight and therefore a smaller

θ_R. More discussion on this will be given later in this section. With further increasing Re, θ_R rises rapidly and approaches a constant, about 79°, beyond $Re = 12\,000$. The observation that θ_R approaches a constant at a large Re is consistent with Wang *et al.*'s (2005) report that, at $\alpha = 45^\circ$ and $\beta = 0^\circ$, rivulets occurred at $\theta_R = 72^\circ$ for $Re = 11\,700$ and moved very slowly with increasing Re until reaching $\theta_R = 82^\circ$ at $Re = 17\,100$. They ascribed the observation to: (i) an increase in drag on the rivulet with increasing Re; (ii) an approximate dependence of the flow separation position on Re ($10^5 \sim 3 \times 10^5$). The dashed line in figure 3 indicates transition from one to two rivulets, where one single or two rivulets occur intermittently. The transition between single and two rivulets occurs in the range of $Re = 1500$–2500 ($U_\infty = 1$–$1.7\,\mathrm{m\,s^{-1}}$) for $\alpha = 80^\circ$ and $Re = 3000$–5200 ($U_\infty = 2$–$3.5\,\mathrm{m\,s^{-1}}$) for $\alpha = 55^\circ$. Lemaitre *et al.* (2006) performed theoretical analysis on the formation of rivulets along an inclined cylinder and found that the critical Re for this transition was proportional to $\sqrt{\cos\alpha}$, that is, the critical Re increased as α decreased, which is fully consistent with the present results. The critical Re estimated from theoretical analysis was 1300 ($0.85\,\mathrm{m\,s^{-1}}$) at $\alpha = 80^\circ$ and 2400 ($1.6\,\mathrm{m\,s^{-1}}$) at $\alpha = 55^\circ$. The deviation of theoretical analysis from experimental data could be attributed to assumptions made in theoretical analysis. A two-dimensional model, along with a prescribed pressure distribution, was used in theoretical analysis. As such, a variation in pressure due to the presence of water rivulets and the effect of water flow along the cylinder were ignored in their model.

The dependence of θ_R on Re is linked to aerodynamic pressure on the rivulet. It is known that aerodynamic pressure varies with U_∞^2. The weight of a rivulet at θ_R along a cable inclined at α may be decomposed into the axial, radial and tangential components, i.e. $mg\sin\alpha$, $mg\cos\alpha\cos\theta_R$ and $mg\cos\alpha\sin\theta_R$, respectively, where m is the mass of water rivulet for a unit length. The axial component, which is independent of θ_R, makes the water rivulet run along the cylinder, and the tangential component tends to pull the rivulet to the leading stagnation line of the cylinder. The tangential component of weight decreases with increasing α but increases with a larger θ_R. The tangential component should be balanced by aerodynamic pressure on the rivulet and tangential friction forces between water and the cylinder surface and between water and air, namely,

$$mg\cos\alpha\sin\theta_R = C_{DR}(h \times 1)\tfrac{1}{2}\rho_a U_\infty^2 + F_{f(c-w)} + F_{f(w-a)}, \qquad (1a)$$

where C_{DR} is the aerodynamic pressure drag acting on the rivulet, ρ_a is the density of air, $F_{f(c-w)}$ is the friction force tangent to the local contact surface between the cylinder and the rivulet per unit axial length, and $F_{f(w-a)}$ is the tangential friction force between the rivulet and air per unit axial length. Applying the 'cosine law' (Ramberg 1983; Hayashi & Kawamura 1995) or the independence principle to calculate the drag yields $C_{DR} = C_{DR}|_{\alpha=90^\circ}\cos(90-\alpha) = C_{DR}|_{\alpha=90^\circ}\sin\alpha$. It is evident that, as α decreases, the values of $mg\cos\alpha$ and C_{DR} increase and decrease, respectively. Based on (1*a*), θ_R reduces for a given U_∞. This is consistent with the intuition that, with decreasing α, the greater the weight of the rivulet that acts to pull the rivulet forward on the cylinder, the smaller θ_R. This will be confirmed later from experimental data. Combining the 'cosine law' and (1*a*) yields

$$mg\cos\alpha\sin\theta_R = C_{DR}|_{\alpha=90^\circ}(h \times 1 \times \sin\alpha)\tfrac{1}{2}\rho_a U_\infty^2 + F_{f(c-w)} + F_{f(w-a)}. \qquad (1b)$$

Equation (1*b*) suggests that a decrease in α corresponds to a decrease in cross-sectional area of the same slug of air and to an increase in $mg\cos\alpha$ and hence to a reduction in θ_R.

The rivulet mass for unit length can be expressed as $m = bh\rho_w$, where $b = A/h$ is the average width of the rivulet. C_{DR} can be estimated from the pressure difference between the two sides of the water rivulet. Given the pressure gradient is constant within the rivulet width b, C_{DR} can be given by $C_{DR} = -\partial C_P/\partial\theta|_{\theta=\theta_R} \times b/0.5d$, where C_P is the pressure coefficient. Assuming $F_{f(c-w)}$ and $F_{f(w-a)}$ to be small relative to C_{DR}, (1*a*) is then reduced to

$$mg\cos\alpha\sin\theta_R = -\left.\frac{\partial C_P}{\partial\theta}\right|_{\theta=\theta_R}\frac{b}{d/2}h\tfrac{1}{2}\rho_a U_\infty^2 \qquad (1c)$$

or

$$\frac{mgd}{bh\rho_a}\cos\alpha\sin\theta_R = -\,U_\infty^2\left.\frac{\partial C_P}{\partial\theta}\right|_{\theta=\theta_R}. \qquad (1d)$$

Equations (1*c*) or (1d) imply that, as θ_R increases with a larger U_∞, the tangential component of the rivulet weight climbs, which is compensated by the greater U_∞ and/or the pressure gradient at the rivulet position. At a smaller α, given a constant θ_R, the tangential component of the weight is larger, and a higher U_∞ is required to maintain the rivulet at the same θ_R, as observed in figure 3.

Experimental data of $\partial C_P/\partial\theta|_{\theta=\theta_R}$ on a cylinder with running water rivulets are not available. As the rivulet thickness ($h^* \approx 0.1$) is very small, compared with the cylinder diameter, it seems reasonable to assume $\partial C_P/\partial\theta|_{\theta=\theta_R}$ to be the same with and without the rivulets. Then, $\partial C_P/\partial\theta|_{\theta=\theta_R}$ may be approximately estiamted from the pressure distribution over a clean cylinder (Thompson 1980), namely,

$$C_P(\theta) = 1-(1-C_{Pm})\times\sin^2\left(\frac{\pi}{2}\frac{\theta}{\theta_m}\right) \quad (0 \leqslant \theta \leqslant \theta_m), \qquad (2a)$$

$$C_P(\theta) = C_{Pb}-(C_{Pb}-C_{Pm})\times\cos^2\left(\frac{\pi}{2}\frac{\theta-\theta_m}{\theta_b-\theta_m}\right) \quad (\theta_m \leqslant \theta \leqslant \theta_b), \qquad (2b)$$

$$C_P(\theta) = C_{Pb} \quad (\theta_b \leqslant \theta \leqslant 180^\circ), \qquad (2c)$$

where C_{Pm}, C_{Pb}, θ_m and θ_b are the minimum pressure coefficient, base pressure coefficient, minimum pressure position and asymptotic base pressure point, respectively. Then,

$$\left.\frac{\partial C_P}{\partial\theta}\right|_{\theta=\theta_R} = -(1-C_{Pm})\frac{\pi}{2\theta_m}\sin\left(\pi\frac{\theta_R}{\theta_m}\right) \quad \text{for } 0 \leqslant \theta_R \leqslant \theta_m, \qquad (3a)$$

$$\left.\frac{\partial C_P}{\partial\theta}\right|_{\theta=\theta_R} = (C_{Pb}-C_{Pm})\frac{\pi}{2(\theta_b-\theta_m)}\sin\left(\pi\frac{\theta_R-\theta_m}{\theta_b-\theta_m}\right) \quad \text{for } \theta_m \leqslant \theta_R \leqslant \theta_b. \qquad (3b)$$

For an inclined cylinder at $\alpha \approx 55^\circ$, C_{Pm}, C_{Pb}, θ_m and θ_b are -1.4, -1.15, 85° and 100°, respectively, for the present *Re* range (Hayashi & Kawamura 1995; Cosentino, Flamand & Ceccoli 2003*b*). These values are close to those for a cylinder normal to incident flow, i.e. $\alpha = 90^\circ$ (Zdravkovich 1997; Mei & Currie 1969).

Figure 4 presents the C_P distribution calculated from the above equations. Now we can explain why the rivulet does not change its position once U_∞ exceeds $5.6\,\mathrm{m\,s^{-1}}$ ($Re = 8400$) at $\alpha = 80^\circ$ and $9\,\mathrm{m\,s^{-1}}$ ($Re = 12\,000$) at $\alpha = 55^\circ$. For a given θ_R, the left-hand side of 1(*d*) is constant. Then an increase on U_∞^2 on the right-hand side would be compensated by a decrease in $\partial C_P/\partial\theta$. For $\theta < \theta_m$, $\partial C_P/\partial\theta$ is negative, along with (3*a*) and (3*b*), implying a positive pressure drag on the rivulet. The pressure gradient increases first from 0 at $\theta = 0^\circ$ to -1.2653 at $\theta = 45^\circ$, and then drops, reaching 0 at $\theta = \theta_m$. In addition, the decrease in $\partial C_P/\partial\theta$ with an increase in θ is substantial around

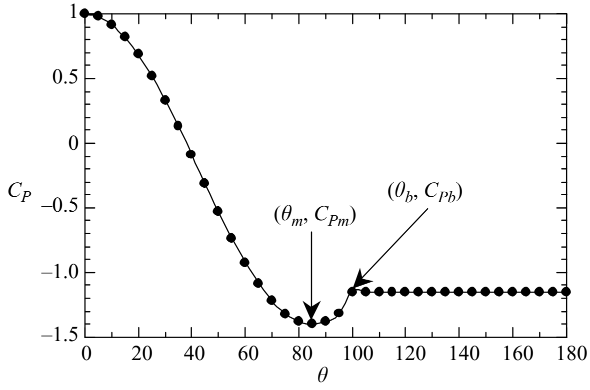

FIGURE 4. Calculated C_P from (2) for $C_{Pm} = -1.4$, $\theta_m = 85°$, $C_{Pb} = -1.15$.

$\theta = \theta_m$, which may be inferred from differentiating 3(a) and 3(b) with respect to θ, i.e. $-\partial^2 C_P/\partial\theta^2$. Therefore, as the rivulet approaches θ_m with further increasing U_∞, an increase in U_∞^2 is compensated, based on (1d), by a large drop in $\partial C_P/\partial\theta$, resulting in the almost constant product, $-U_\infty^2 \partial C_P/\partial\theta|_{\theta=\theta_R} = (mgd/bh\rho_a)\cos\alpha\sin\theta_R$, and hence no appreciable change in θ_R with increasing U_∞. The rivulet can never reach $\theta = \theta_m$ because $\partial C_P/\partial\theta$ is zero at $\theta = \theta_m$, implying a zero pressure drag on the rivulet and hence no force (except friction forces) to balance the tangential component of the rivulet weight. The friction forces, between water and cylinder surface, and between water and air, neglected in the above analysis should not be sufficiently large, as will be seen later in this section, to balance this component. It is worth mentioning that the modified pressure distribution due to the presence of water rivulets is not considered in the above analysis.

Plugging $\partial C_P/\partial\theta|_{\theta=\theta_R} = -(1 - C_{Pm})\frac{\pi}{2\theta_m}\sin(\pi\theta_R/\theta_m)$ and $m = bh\rho_w$ in to (1c) yields

$$\frac{\rho_w g(d/2)}{\pi\rho_a} = C_c = (1 - C_{Pm})\frac{1}{4\theta_m}U_\infty^2\frac{\sin\left(\pi\frac{\theta_R}{\theta_m}\right)}{\cos\alpha\sin\theta_R} \quad (0 \leqslant \theta_R \leqslant \theta_m), \tag{4}$$

where C_c is a constant associated with constant parameters g, ρ_w, ρ_a and $d/2$ for a given cylinder diameter, and the units are $\mathrm{m}^2/\mathrm{s}^{-2}$, which are the units of the potential or kinetic energy per unit mass. The left-hand side of (4) is connected to the potential (gravitational) energy of the rivulet due to lifting the rivulet upward. The right-hand side is associated with the kinetic energy of the free-stream flow per unit mass.

Figure 5 shows the dependence of C_c on Re, calculated from the right-hand side of (4), and divulges that C_c is almost constant, about 21. On the other hand, the value obtained from the left-hand side is 27, greater than that on the right-hand side. The deficit is ascribed to neglecting the friction force terms in (4) and/or using the θ_m and C_{Pm} values for a clean cylinder, which should be modified in the presence of the rivulets. The deficit is small, about 6 %, at $Re = 6800$ and $\alpha = 80°$, and 15 % at $Re = 9600$ and $\alpha = 55°$. As discussed earlier, the rivulets oscillate significantly at these Re values. The friction force of a moving rivulet is always smaller than that of a stationary rivulet because the kinetic friction coefficient is always less than the static. As a result, the time-averaged friction forces of oscillating rivulets will be smaller than that of non-oscillating rivulets. It may be concluded that the friction force $(F_{f(c-w)} + F_{f(w-a)})$ acting on a rivulet is around 22 % (= ((27 − 21)/27) × 100 %) of the total force on the rivulet.

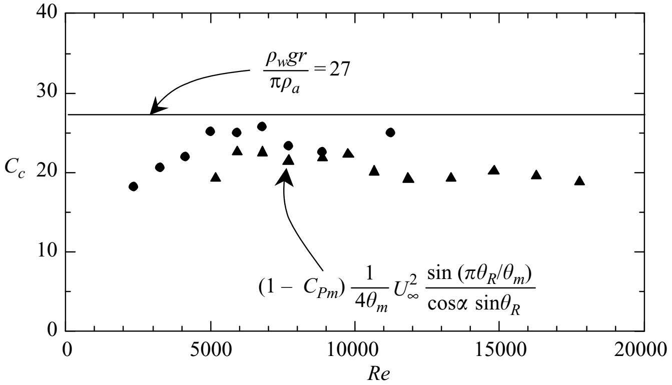

FIGURE 5. Deficit between the potential (gravitational) energy of the rivulet $\rho_w g(d/2)/\pi\rho_a$ and the kinetic energy of free-stream flow per unit mass $(1 - C_{Pm})(1/4\theta_m)U_\infty^2 \frac{\sin(\pi\theta_R/\theta_m)}{\cos\alpha \sin\theta_R}$. U_∞ and θ_R are experimental, given in figure 3. ●, $\alpha = 80°$; ▲, $\alpha = 55°$.

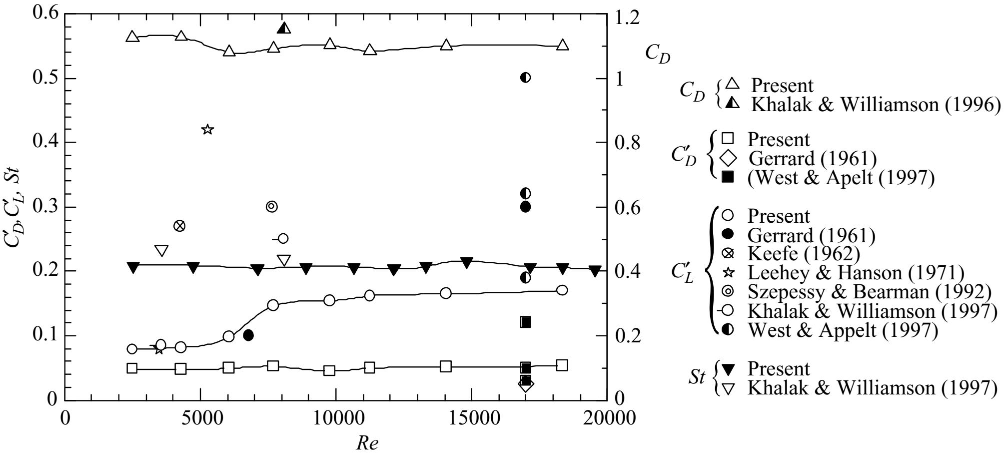

FIGURE 6. Forces and Strouhal number for a cylinder normal to incident flow ($\alpha = 90°$).

4. Fluid forces

4.1. *Force measurement validation*

Figure 6 shows the dependence on Re of time-averaged drag (C_D), fluctuating drag (C'_D) and lift (C'_L), and St at $\alpha = 90°$ in the absence of water. The prime denotes the r.m.s. value. C_D, C'_D and St are about 1.1, 0.05 and 0.207, respectively, for $Re = 2.6 \times 10^3$–2.2×10^4; C'_L is small, about 0.09, at $Re = 2.6 \times 10^3$–7×10^3 and 0.15 at $Re = 8 \times 10^3$–2.2×10^4. The data in the literature are also given in the figure. There is scattering among data, which is probably due to different experimental conditions. Table 1 gives some experimental details of the data. It is well known that C_D, C'_L, C'_D and St are all dependent on experimental conditions such as Re, turbulent intensity, blockage, aspect ratio and end effects (Surry 1972; Laneville, Gartshore & Parkinson 1975). Since the forces are measured for the full length of the cylinder and the flow velocity near the tunnel wall is smaller than in the free stream, the present measurement of C_D is 0.9 %, 2.7 %, 3.6 % and 7.2 % below that measured by Nebres & Battill (1993), Ting *et al.* (1998), Khalak & Williamson (1996) and Lesage &

	Reynolds number	Turbulent intensity (%)	Measurement technique	C_D	C'_D	C'_L	St
Gerrard (1961)	8×10^3	0.3	Sectional (pressure distribution)	–	–	0.1	–
	2×10^4			–	0.025	0.3	–
Keefe (1962)	5×10^3	0.3	On $1D$ (loadcell)	–	–	0.27	–
Protos *et al.* (1968)	4.5×10^4	–	On full length, $11D$	–	–	0.28	–
Leehey & Hanson (1971)	4.1×10^3	0.04	Sectional (acoustic)	–	–	0.08	–
	6.2×10^3					0.42	–
Lesage & Gartshore (1987)	6.5×10^4	–	Sectional (pressure distribution)	1.19	–	0.45	–
Szepessy & Bearman (1992)	9×10^3	0.05	Sectional (pressure distribution)	–	–	0.3	–
Nebres & Battill (1993)	3×10^4	0.06	Sectional (press distribution)	1.12	–	–	–
Khalak & Williamson (1996)	4.2×10^3	–	On full length, $10D$ (force balance)	–	–	0.085	0.235
	9.5×10^3			1.15	–	0.25	0.23
West & Appelt (1997)	2×10^4	0.2	Sectional (pressure distribution)	–	0.12	0.5	–
			On $15D$ (correlation length)	–	0.05	0.32	–
			On $50D$ (correlation length)	–	0.03	0.19	–
Ting *et al.* (1998)	6.8×10^4	0.8	Sectional (pressure distribution)	1.14	–	–	–
Alam *et al.* (2003*c*)	5.5×10^4	0.5	On $0.92D$ (loadcell)	1.12	0.14	0.48	0.186
Present	$(2.6\text{–}7) \times 10^3$	0.7	On the full length, $13D$ (loadcell)	1.1	0.05	0.09	0.207
	$(0.8\text{–}1.3) \times 10^4$			1.1	0.05	0.13	0.207

TABLE 1. Fluid force coefficients and Strouhal numbers of a circular cylinder.

Gartshore (1987), respectively. Based on their measurements, West & Apelt (1982) suggested that the blockage had virtually no effect on C_D if it was less than 6 % and could have a very small effect if it was between 6 % and 7.5 %. Therefore, the present blockage (7.5 %) is expected to have a negligible effect on C_D.

There is a relatively large scattering in C'_D and C'_L, which are highly sensitive to experimental conditions. West & Apelt's (1997) data in table 1 clearly indicates that C'_D and C'_L on an elemental section are independent of spanwise location for an aspect ratio exceeding 10, though dependent on the measurement length of the cylinder (West & Apelt 1997; Norberg 2001). C'_L and C'_D tend to be on the large side when measured at a section and to decrease with an increasing measurement length. The present C'_L and C'_D on the full length of the cylinder are slightly lower than those measured at a section or over a finite-length cylinder, and are very close to those measured on the full length of a cylinder (table 1).

The present St, 0.207, is in good agreement with others. The above comparison provides a validation for the present measurements.

4.2. $\alpha = 80°$

Figure 7 shows C_D, C'_D and C'_L at $\alpha = 80°$ with and without running water rivulets. As Re increases, C_D at $\alpha = 80°$ in the absence of water behaves rather similarly to that at $\alpha = 90°$ (figure 6), following the 'cosine law', i.e. $C_D(\alpha = 80°) = C_D(\alpha = 90°) \times \cos$

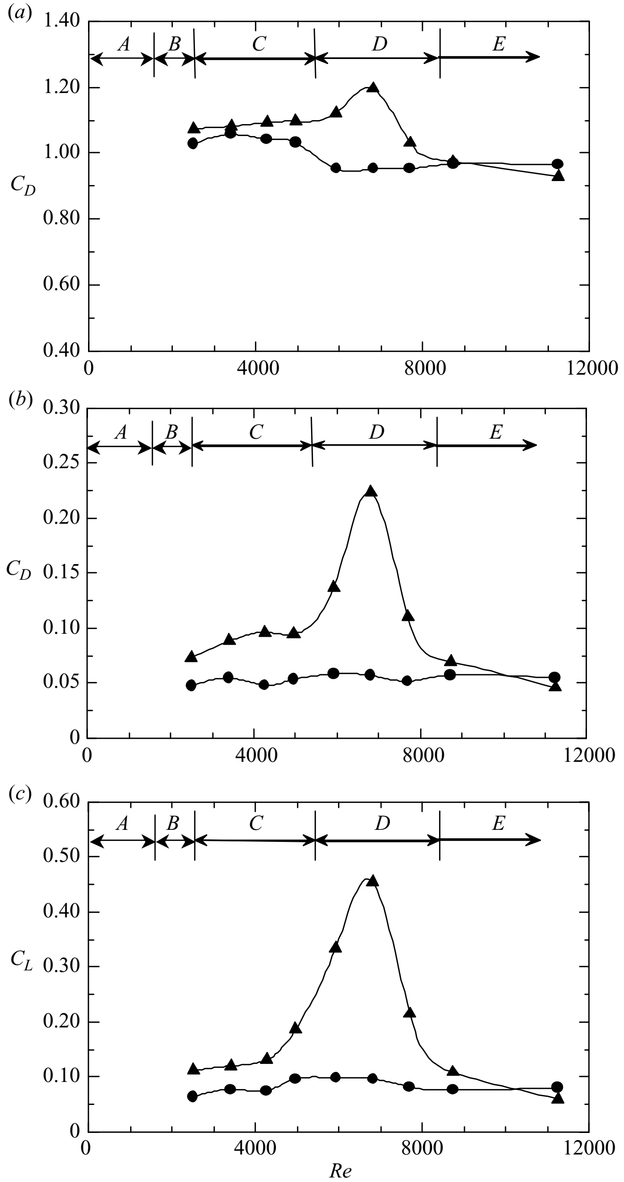

FIGURE 7. Effect of running water rivulets ($\alpha = 80°$) on (a) C_D, (b) C'_D and (c) C'_L. ●, without water; ▲, with water.

(90–80)°. The validity of the 'cosine law' for an inclined cylinder is previously well documented for C_D, but not for C'_D and C'_L to our knowledge. In the absence of water, $C'_D(= 0.05)$ at $\alpha = 80°$ is the same as $\alpha = 90°$. On the other hand, C'_L at $\alpha = 80°$ is about 0.09 for the range of Re examined, but C'_L at $\alpha = 90°$ is 0.09 at $Re = 2.6 \times 10^3$–7×10^3 and 0.15 at $Re = 8 \times 10^3$–2.2×10^4. It is evident that the 'cosine law' is not applicable for calculating fluctuating forces, which will be re-confirmed later at $\alpha = 55°$.

In the presence of running water rivulets, the variations of C_D, C'_D and C'_L with Re are very different from those without water, which is particularly evident in the range of $Re = 5300$–8400. The fluid forces (C_D, C'_D and C'_L) are linked with θ_R. A

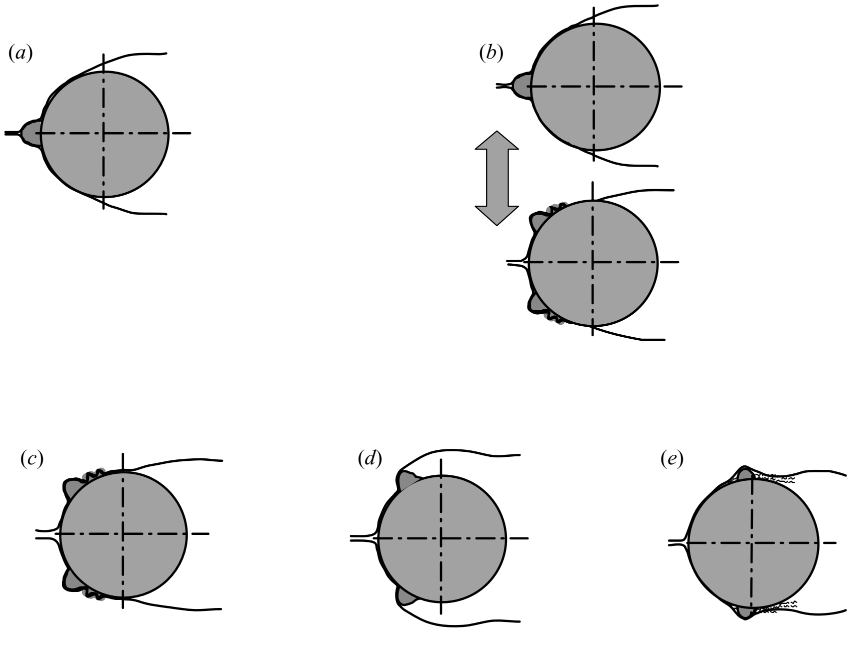

Figure 8. Sketch of the dependence of flow separation on the rivulet position.

change in Re leads to a different rivulet position (figures 2 and 3) and subsequently a variation in C_D, C'_D and C'_L . Five distinct behaviours of the rivulets and forces may be identified, corresponding to five Re ranges or flow categories, as marked at the top of each plot in figure 7.

The five flow categories, referred to as A, B, C, D and E, are sketched in figure 8. The classification is made based on the position of water rivulets, which has a profound effect on the fluid forces and St. In Category A (figure 8*a*), Re is smaller than 1500 (cf. figure 3) and only one single water rivulet occurs along the leading stagnation line. Category B (figure 8*b*) corresponds to $Re = 1500$–2500 (marked by the dashed line in figure 3), where both one and two rivulets may occur and switch from one to another intermittently. The forces were not measured in Categories A and B because (i) the influence of water rivulets at the leading stagnation line on forces and flow structure is expected to be very small (Nebres & Batill 1993), and (ii) aerodynamic forces are very small at low flow velocities, which could not be resolved by the load cell used.

In Category C (figure 8*c*), Re is in the range 2500–5300, and water rivulets occur between the leading stagnation and flow separation lines. The fluid forces on the cylinder are slightly greater than those without the rivulets. Apparently, the influence of the rivulets on the forces is limited; the boundary layers remain attached behind the rivulets. Alam *et al.* (2003*a*) observed this kind of flow structure when placing two tripping wires at $\theta_R = 20°$–$40°$ on a cylinder normal to incident flow. The reattachment of the boundary layer behind the rivulets caused some ripples of water behind the rivulets, as observed in figure 2(a, b). In this range of Re, water rivulets occur at $\theta_R = 28°$–$60°$ (figure 3), and C_D, C'_D and C'_L all increase, compared with a clean cylinder, which is probably, at least partially, due to the increased effective height of the cylinder in the presence of the rivulets.

In Category *D* (figure 8*d*), *Re* is between 5300 and 8400, and the two rivulets move further downstream, with θ_R in the range 60°–78°. It is likely that the boundary layers may separate from the rivulets earlier than in the absence of the rivulets, thus leading to an increase in C_D, C'_D and C'_L (figure 7). At $Re = 6800$, C_D, C'_D and C'_L all display a pronounced peak, with C'_D and C'_L reaching 4.25 and 5.75 times, respectively, their counterparts in the absence of the water rivulets. There are three possible causes for the pronounced rise in C_D, C'_D and C'_L:

(i) The rivulets oscillate along the circumference of the cylinder, probably resulting from the oscillation of flow separation lines. It has been previously suggested that the oscillation of the rivulets may magnify the aerodynamic forces and lead to a modified excitation mechanism (e.g. Flamand 1995; Matsumoto *et al.* 1995, 2005*a*, *b*; Verwiebe & Ruscheweyh 1998; Burton *et al.* 2005). Burton *et al.* (2005) simulated numerically the time-averaged drag on a two-dimensional cable with an oscillating water rivulet on the circumference of the cable for $\theta_R = 20°–70°$ and found that the cable experienced a maximum time-averaged drag for $\theta_R = 60°–70°$, though the fluctuating forces were not reported.

(ii) The occurrence of the rivulets induces early flow separation. It is known that alternate vortex shedding induces out-of-phase pressure fluctuations on the two opposite sides of a cylinder, and a higher pressure fluctuation occurs in the region from the separation point to the base point, with the highest at the separation point (Son & Hanratty 1969; Batham 1973; Alam *et al.* 2003, 2005). Therefore, the early separation of the boundary layer due to the rivulets amplifies the high-pressure fluctuation region, contributing at least partially to the higher C'_L and C'_D. The association between the rivulets and the flow separation also provides an explanation for the observed significant oscillation of water rivulets. Alam *et al.* (2003*b*) noted that the positions of the tripping wires on the circumference of a cylinder greatly influenced C_D, C'_D and C'_L, which rose significantly when the boundary layer separates from the wires at $\theta_R = 60°$. The flow pattern in their report closely resembles figure 8(*d*).

(iii) The running water rivulets enhance the two-dimensionality of vortex shedding and hence the coherence of vortices, which will be elaborated later.

In Category *E* (figure 8*e*), the rivulets shift further downstream and appear straight again along the cylinder (figure 2*e*, 2*f*). Igarashi (1986) reported that, when two tripping wires were placed directly behind the flow separation lines on a circular cylinder, the shear layers behind the tripping wires were highly turbulent, leading to weakened vortex shedding, lower drag and higher *St* (see also Naumann & Quadflieg 1972; Kareem & Cheng 1999). It is plausible that the rivulets occur probably directly behind the flow separation line, and act as the stabilizer of the shear layers, resulting in postponed flow separation and hence smaller fluctuating fluid forces (figure 7). The flow structure in this category could resemble that on a circular cylinder at the early stage of the critical-Reynolds-number range (Farrel & Blessmann 1983; Schewe 1983; Almosnino & McAlister 1984; Higuchi, Kim & Farell 1989).

4.3. $\alpha = 55°$

Figure 9 presents C_D, C'_D and C'_L at $\alpha = 55°$ with and without running water rivulets. In the absence of water, C_D varies little with *Re* (figure 9*a*). The measured C_D at $\alpha = 55°$ is about 0.87. However, the 'cosine law' gives $C_D(\alpha = 90°) \times \cos\,(90–55°) = 0.90$. Furthermore, C'_D and C'_L are 0.06 and 0.1, respectively, and those from the 'cosine law' are 0.049 and 0.073. Evidently, the 'cosine law' is invalid at $\alpha = 55°$, not only for C'_D and C'_L, but also for C_D. It will be confirmed later that *St* also follows the cosine law for $\alpha = 80°$, but not for $\alpha = 55°$. In fact, the 'cosine law' is valid

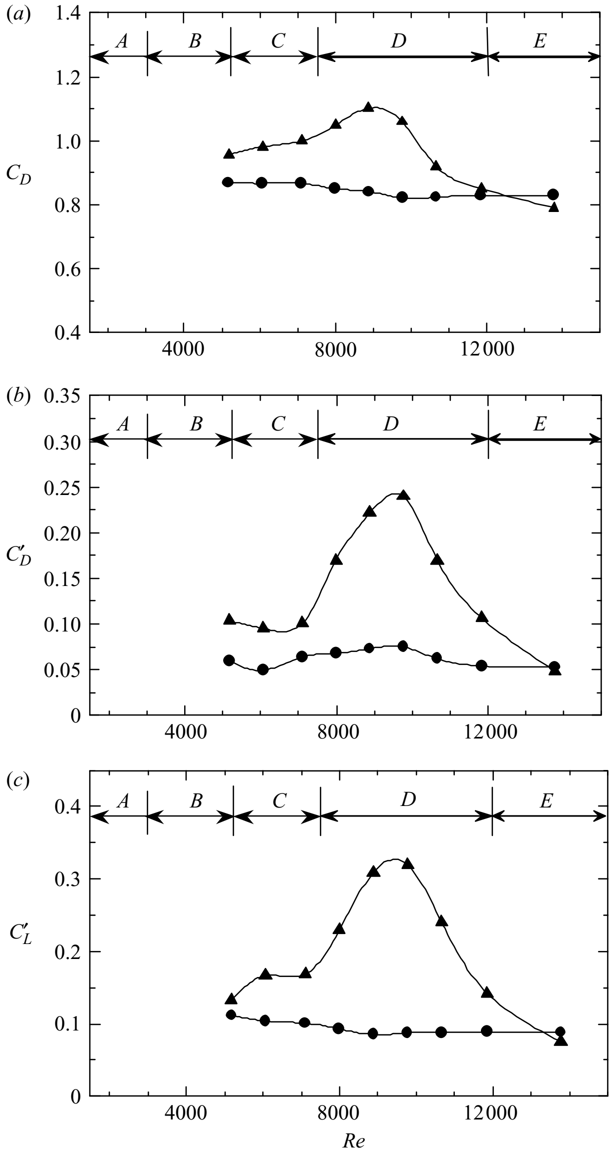

FIGURE 9. Effect of running water rivulets ($\alpha = 55°$) on (a) C_D, (b) C'_D and (c) C'_L. ●, without water; ▲, with water.

only for a highly inclined cylinder, i.e. $\alpha = 65°–90°$ (Bursnall & Loftin 1951; Van Atta 1968; Ramberg 1983). The quoted C_D, C'_D and C'_L are the averaged values over the Re range shown in figure 9. In the presence of water rivulets, C_D, C'_D and C'_L behave similarly to those at $\alpha = 80°$ (figure 7), though their maximum occurs at $Re = 9600$, which is higher than its counterpart ($Re = 6800$) at $\alpha = 80°$. The corresponding θ_R is 67°, smaller than 70° as at $\alpha = 80°$. This is reasonable. At a larger angle between the gravity force of water and the cylinder axis, a flow velocity higher than that at $\alpha = 80°$ is required in order to lift the rivulets to $\theta_R = 67°$. The variation in C_D, C'_D and C'_L with Re is again classified into five categories, i.e. A, B, C, D and E, the corresponding Re ranges being 0–3000 (single rivulet, $\theta_R \approx 0°$), 3000–5200 $\mathrm{m\,s^{-1}}$ (transition from one to two rivulets, $\theta_R \approx 0°–18°$), 5200–7400 (two rivulets at $\theta_R = 18°–50°$), 7400–12 000 ($\theta_R = 50°–74°$) and >12 000 ($\theta_R \approx 78°$), respectively. Note that Category *D* spreads over a larger *Re* range than that at $\alpha = 80°$, consistent with Gu & Du's (2005) report that the range of *Re*, where the RWI vibration occurred, became larger for a smaller α. In this category, the maximum C'_D and C'_L with running water rivulets are respectively, 4.7 and 3.3 times, their counterparts without water. Note that the maximum C'_D at $\alpha = 55°$ is larger than that at $\alpha = 80°$, but the maximum C'_L is smaller.

Yamaguchi (1990) and Matsumoto *et al.* (2005*b*) investigated the effect of an artificial rivulet position on the time-averaged drag on a cable and noted that this drag reached the maximum with the rivulet placed at 70°. Matsumoto *et al.* (1995) observed that a cable became aerodynamically unstable when the upper rivulet reached $\theta_R = 60°–75°$ for $\alpha = 40°$ and $\beta = 45°$. The rivulet position, at which Yamaguchi (1990), Matsumoto *et al.* (1995, 2005*b*) and Burton *et al.* (2005) observed the maximum drag/instability, is close to the present observation.

Matsumoto *et al.* (2005*a*) investigated experimentally the effect of water rivulet oscillation on the aerodynamic stability of a cable model. The oscillation of the water rivulet synchronizing with the cable vibration was simulated by the rotational oscillation of the cable with a fixed artificial rectangular-shaped rivulet, with a phase shift (ϕ) between the rivulet and cable oscillations from 0° to 315°. They concluded that the oscillation of water rivulets enhanced the unsteady force and cable vibration for a certain range of θ_R, which is consistent with the present results.

5. Flow behind the cylinder

5.1. *Dominant vortex frequency*

Figure 10 compares *St* in the presence of water with that in the absence of water. For the inclined cylinder at $\alpha = 80°$, the averaged *St* over $Re = 2200–11\,200$ (figure 10*a*) is about 0.197 without water (figure 10*a*), smaller than that (0.207) at $\alpha = 90°$ (figure 6). This is reasonable because the component, normal to the cylinder, of free-stream velocity at $\alpha = 80°$ is smaller than at $\alpha = 90°$, that is, *St* follows the cosine law, $St(\alpha = 80°) = St(\alpha = 90°) \times \cos(90–80°) = 0.2$, close to the measurement, confirming the independence principle (Ramberg 1983). Note that *St* rises, albeit slowly, with increasing *Re*.

At $\alpha = 55°$ (figure 10*b*), the variation in *St* with *Re* is more significant without water than with water, but the trend is in general opposite to that at $\alpha = 80°$, irrespective of the presence or absence of water. Ramberg (1983) noted a large scattering in the measured *St* of a clean cylinder at $\alpha = 30°–75°$ as *Re* changed from 210 to 1100. A possible dependence of the *St–Re* relationship on α or the cylinder cross-section could be responsible for this observation.

In Category *C*, where *Re* is relatively small, *St* in the presence of water is slightly smaller than in the absence of water since two symmetrical rivulets occur near the leading stagnation line and have a small effect on fluid dynamics. However, in Category *D*, *St* at a given *Re* drops substantially owing to the presence of water, compared with that in the absence of water. The observation conforms to reports (Roshko 1954; Bearman & Trueman 1972; Fox & Apelt 1993; Norberg 2003) that a drop in *St* is in general associated with an increase in the vortex strength and mean and fluctuating fluid forces on a cylinder. In the free vibration of an elastic circular cylinder in cross-wind, synchronization begins when f_s coincides with the natural frequency (f_n) of the cylinder and ends at about $f_s/f_n \approx 1.4$ (Sarpkaya 1979), that is, the lock-in between an oscillating cylinder and vortex shedding may result in the frequency of vortex shedding

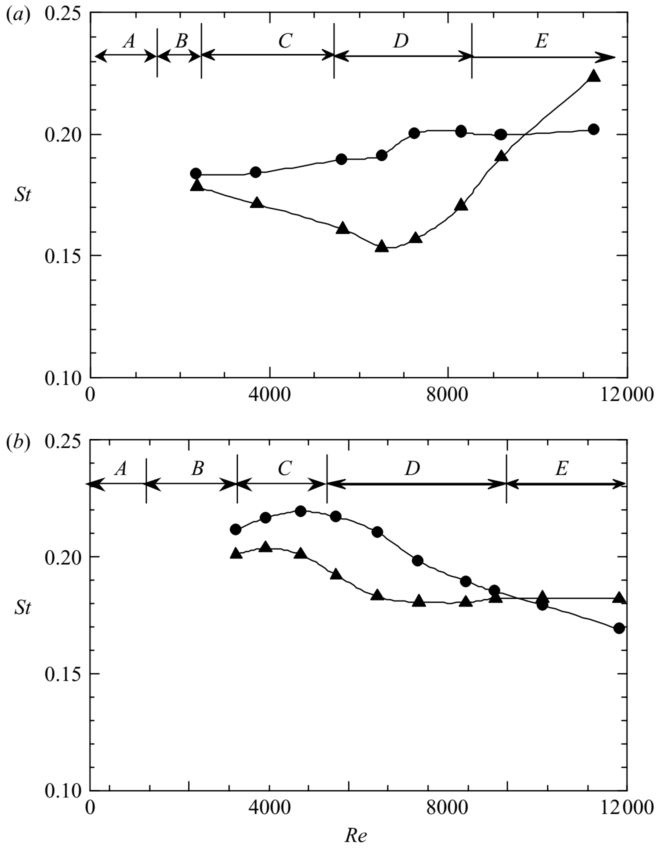

FIGURE 10. Effect of running water rivulets on St: (a) $\alpha = 80°$ and (b) 55°. ●, without water; ▲, with water.

being lower than that associated with a stationary cylinder. Here, the cylinder is considered to be stationary. However, the rivulets are oscillating. The lock-in between the rivulet oscillation and vortex shedding cannot be excluded. In fact, as will be seen later in this section and § 6, all the present data of the flow and forces point to the occurrence of this lock-in, which is probably responsible for the falling St. In Category E, St increases with the presence of rivulets; meanwhile, C_D, C'_D and C'_L (figures 7 and 9) all decrease.

The trend in the variation of St with Re tends to be opposite to that of C_D (figures 7a, 9a). For a plain circular cylinder, Goldstein (1965) and Roshko (1952) observed that C_D is inversely proportional to St. A compilation of the C_D and St data collected by Zdravkovich (1997) for a circular cylinder ($\alpha = 90°$) gave $C_D St \approx 0.21$ for $Re = 3 \times 10^2$–3×10^5. The invariance of $C_D St$ is reconfirmed for the clean cylinder at $\alpha = 90°$, with $C_D St \approx 0.23$ (figure 11). For the cylinder inclined at $\alpha = 80°$, C_D St is maintained at 0.185, whether water is present or absent; at $\alpha = 55°$, the $C_D St$ values collapse, in spite of a considerable variation in C_D (figures 7a, 9a) and St (figure 10) with Re, with those at $\alpha = 80°$ for $Re < 8900$, though dipping appreciably for $Re > 8900$.

Figure 12 presents the power spectral density functions, E_u and E_L, of the hot-wire-measured fluctuating streamwise velocity (u) and the fluctuating lift force (L)

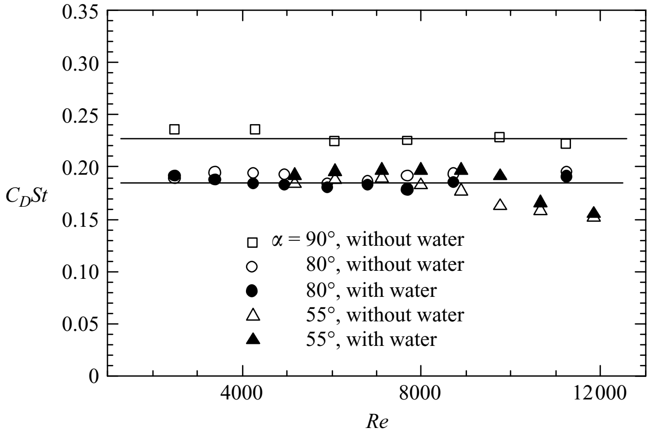

FIGURE 11. Invariance of C_DSt with a change in Re.

measured by a load cell for $\alpha = 80°$ and 55°. E_u or E_L, calculated using a fast Fourier transform algorithm, were determined based on the average of 15 runs, each composed of 1024 samples. Both E_u and E_L display one pronounced peak at the same frequency. Note that the energy at frequencies higher than f_s is significantly higher in E_u than that in E_L, indicating that the hot-wire signal could capture more information on the eddies of high frequencies or smaller scales than the lift force signal. The differences in St and the magnitude of the pronounced peak in E_u or E_L are small in Category C (figures 12a, b, g, h), confirming the small influence of the water rivulets on St and the strength of the vortices in this flow category. The differences are, however, pronounced in Categories D and E. In Category D (figure 12c, d, i, j), compared with that in the absence of water, the major peak in E_u or E_L appears at a lower frequency but more pronounced, indicating a higher energy concentration. In Category E (figure 12e, f, k, l), St climbs, even exceeding that for the clean cylinder; the spectra display a broader and less sharp peak than without water rivulets.

The spectral coherence (Coh_{uL}) between u and L provides a measure of correlation between the two signals at various frequencies. A pronounced peak occurs in Coh_{uL} (figure 13) at f_s, the same as E_u and E_L (figure 12), that is, vortex shedding and the fluctuating lift are highly correlated. The peak in Category D (figure 13d, j) is remarkably higher, about four and three times that without water at both $\alpha = 80°$ and 55°. This peak is also much more pronounced than that at Categories C (figure 13b, h) or E (figure 13f, l). As discussed earlier, Category D is characterized by the presence of oscillating rivulets. It is probably the rivulet oscillation in Category D that enhances greatly the correlation between vortex shedding and fluctuating lift. One possible scenario is that the rivulet oscillation (or its harmonics) and the flow separation (and hence the fluctuating lift) are synchronized or locked in with each other, thus resulting in the greatly increased fluctuating lift and Coh_{uL} at f_s. There will be more discussion on this in §6. Note that the major peak in Category E (figure 13f, l) is even weaker than in the absence of water, suggesting along with E_u and E_L (figure 12) very weak vortex shedding and fluctuating lift, reinforcing our earlier proposition that the rivulets in this flow category act as the stabilizer of the shear layers, and the flow structure could resemble that on a circular cylinder at the early stage of the critical flow regime.

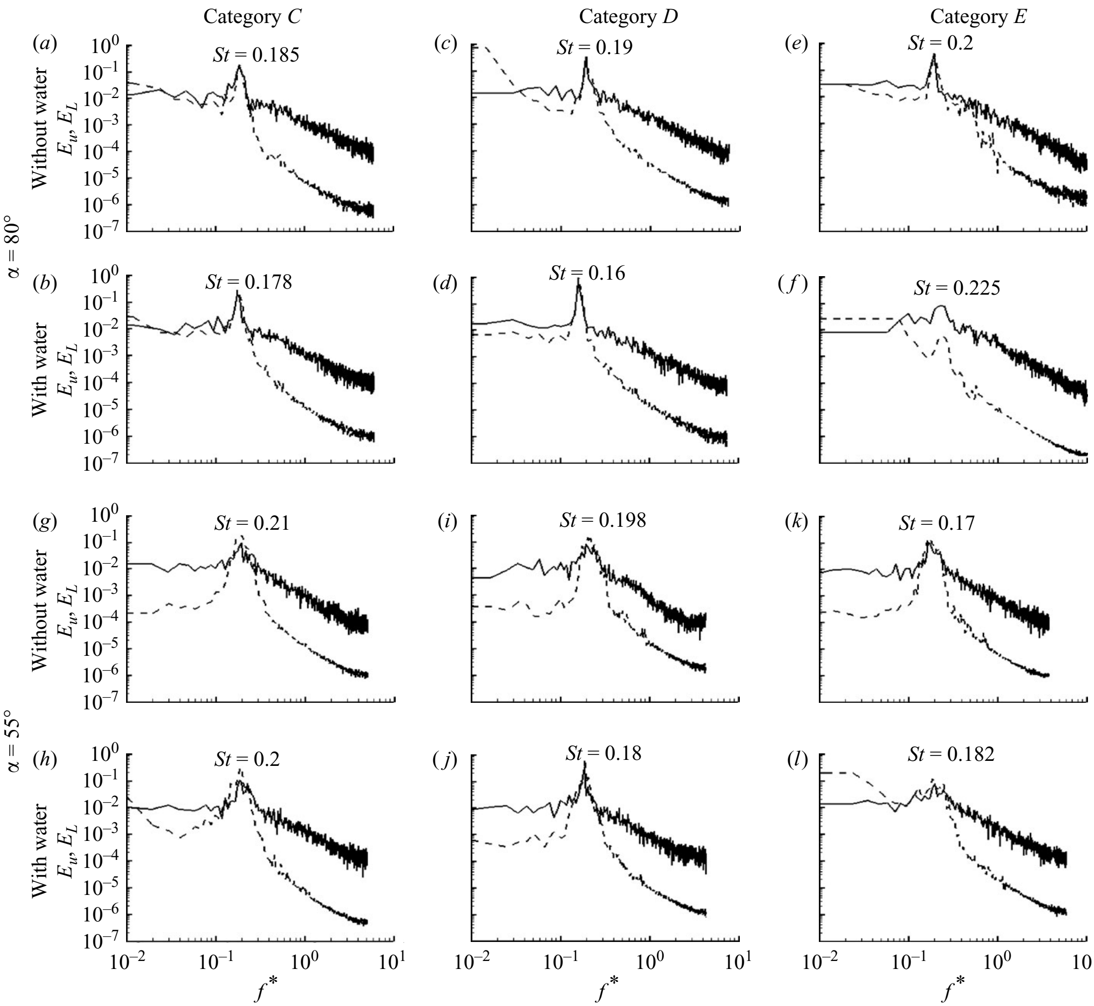

FIGURE 12. The power spectral density functions, E_u (solid line) and E_L (dashed line), of the streamwise fluctuating velocity u and fluctuating lift L at $\alpha = 80°$ and $55°$: (*a*), (*b*) $Re = 3800$; (*c*), (*d*) 6800; (*e*), (*f*) 11 200; (*g*), (*h*) 5200; (*i*), (*j*) 9600; (*k*), (*l*) 15 000.

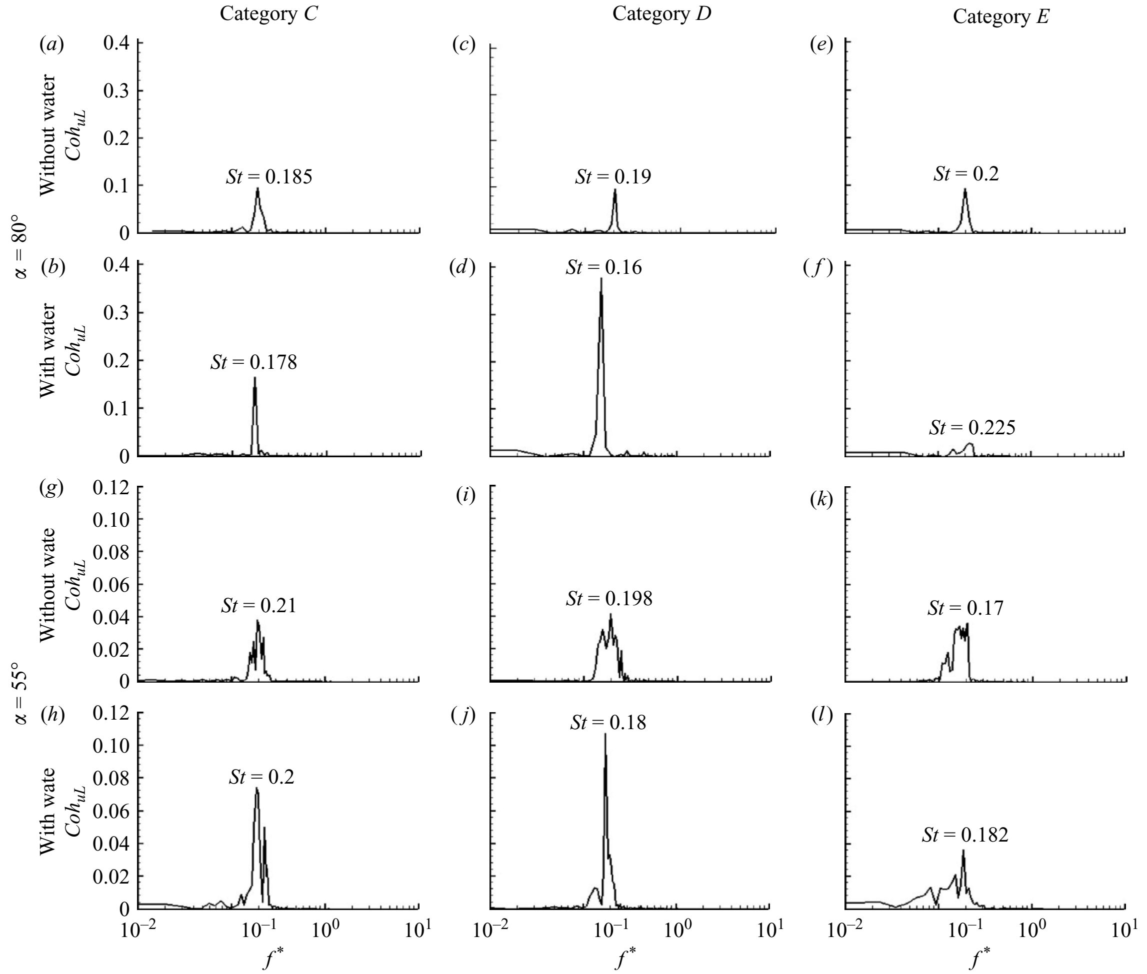

FIGURE 13. Spectral coherence Coh_{uL} between the fluctuating lift force and streamwise fluctuating velocity at $\alpha = 80°$ and $55°$: (*a*), (*b*) $Re = 3800$; (*c*), (*d*) 6800; (*e*), (*f*) 11 200; (*g*), (*h*) 5200; (*i*), (*j*) 9600; (*k*), (*l*) 15 000.

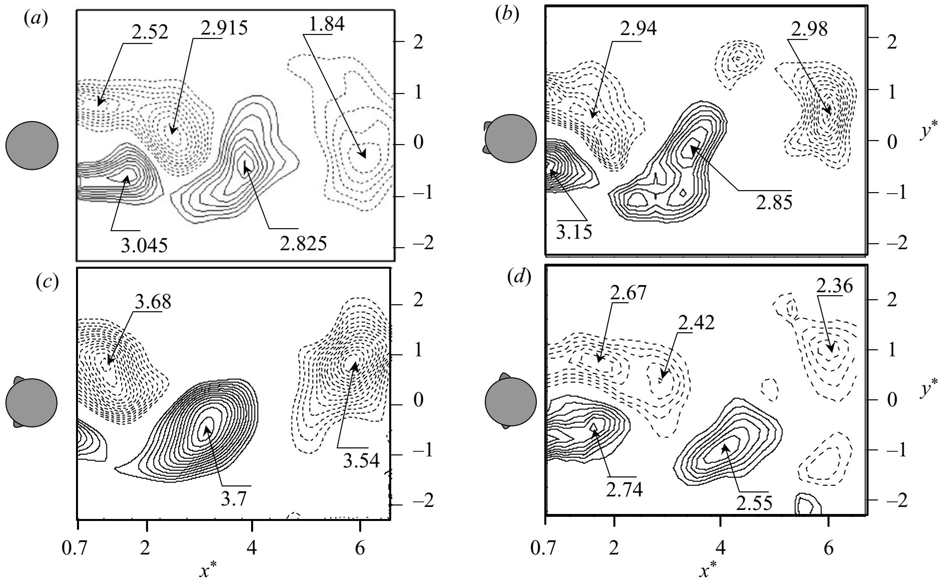

FIGURE 14. Instantaneous vorticity contours $\omega_z^* = \omega_z d/U_\infty$ at $\alpha = 80°$: (*a*) without water ($Re = 6800$); (*b*) Category *C* ($Re = 3800$); (*c*) Category *D* ($Re = 6800$); (*d*) Category *E* ($Re = 11\,200$). ——, positive and - - -, negative vorticity contours. The level of the outer contour is about 80% of the maximum ω_z^*.

5.2. *Flow behind the cylinder*

5.2.1. *Vorticity and wake*

Phase-locked PIV images may provide information on the wake of the cylinder for different categories. The pressure signal near the separation point may be used for the required reference phase (e.g. Cantwell & Coles 1983). This technique is difficult to implement as a pressure tap may be blocked by flowing water on the cylinder surface. Davis (1976), Kiya & Matsumura (1988), Matsumura & Antonia (1993), Zhou *et al.* (2002) and Zhou & Yiu (2006) extracted the phase information from the signal of a hot wire, locally placed in the irrotational region outside the wake, and successfully separated coherent and incoherent flow fields. Hu, Zhou & Zhou (2006) developed a phase-locked PIV measurement technique based on triggering of a hot-wire signal measured in the wake of a square cylinder. A similar technique was used here, with a hot wire placed at $x^* = 6$ and $y^* = 3$, to obtain the phase-locked PIV data.

Figures 14 and 15 present the contours of instantaneous vorticity $\omega_z^* = \omega_z d/U_\infty$ calculated from phase-locked PIV images at $\alpha = 80°$ and 55°, respectively. The data are shown for flow categories *C*, *D* and *E*, together with the case of a clean cylinder. In the absence of water, the antisymmetric vortex street is evident for both α values. The maximum ω_z^* decreases from 3.045 at $\alpha = 80°$ to 2.15 at $\alpha = 55°$. Hu *et al.* (2006) measured ω_z^* in the wake of a clean cylinder of $\alpha = 90°$ at $Re = 2600$ and observed a maximum ω_z^* of 3.06, which is consistent with the extrapolation of the present data. The observation is connected to the fact that a lower α corresponds to a lower normal flow velocity and a higher axial flow velocity. The axial flow velocity in general acts to impair the two-dimensionality of the wake, and hence the vorticity strength.

A number of observations can be made based on the phase-locked ω_z^* contours. First, the maximum ω_z^* in Category *D* is largest of all, regardless of α; it is 3.54 at

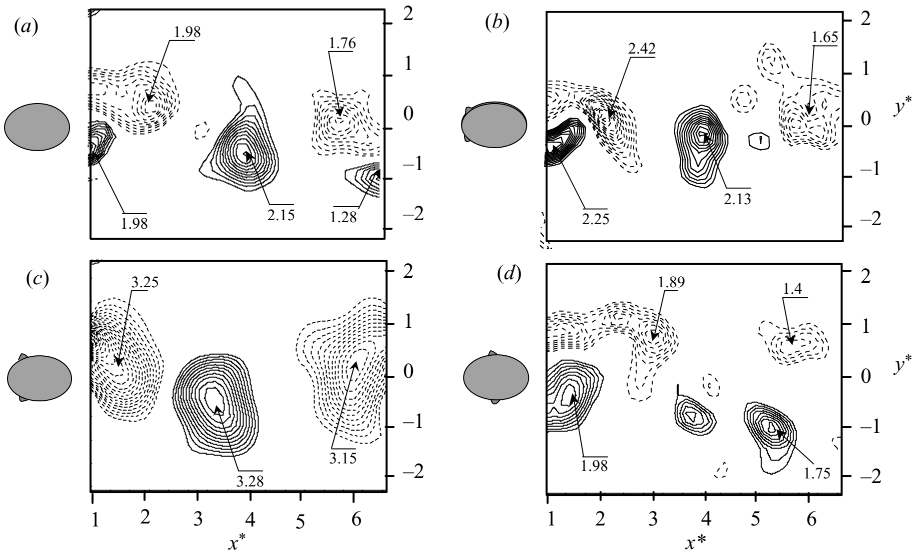

FIGURE 15. Instantaneous vorticity contours $\omega_z^* = \omega_z d/U_\infty$ at $\alpha = 55°$: (*a*) without water ($Re = 9600$); (*b*) Category *C* ($Re = 5200$); (*c*) Category *D* ($Re = 9600$); (*d*) Category *E* ($Re = 15\,000$). ——, positive and - - -, negative vorticity contours. The level of the outer contour is about 80 % of the maximum ω_z^*.

$\alpha = 80°$, significantly higher than its counterparts, 2.98, 2.36 and 1.84, in the other three cases. Secondly, the maximum ω_z^* in Category *E* is smallest for either α. Thirdly, vortices in Category *D* appear most periodical and largest in size of all, whilst those in Category *E* are least periodical and smallest. The observations conform to the observation that C_D, C_D' and C_L' in Category *D* are largest and those in Category *E* are smallest. Finally, the vortex wavelength in Category *D* is longest, consistent with the corresponding small *St*.

Small-scale Kelvin–Helmholtz (K-H) vortices existing in the separating shear layer may have an influence on the growth of the large-scale Kármán vortex. The formation region ($x^* < 0.7$) of the K-H vortices could not be included in the PIV image because of excessive reflection of the laser sheet in close proximity of the cylinder (in spite of a black cylinder surface), which causes significant noises in the PIV data. In order to investigate the K-H vortices and their influences on large-scale vortices, the same PIV system was used for flow visualization at the same flow condition. Smoke generated from paraffin oil was released from two 0.75 mm diameter pinholes symmetrically drilled at about ±35°, respectively, from the nominal leading stagnation point at the mid-span of the cylinder. The particle images were taken using a CCD camera (HiSense type 13, 4M 8 bit, 2048 × 2048 pixels). The Dantec FlowMap Processor (PIV2100 type) was used to synchronize image taking and illumination. Figures 16 and 17 present typical photographs from flow visualization. The photographs in the first, second and third columns show, respectively, the flow of different categories, small-scale K-H vortices in the shear layer ($x^* = 0$–1, $y^* = 0.5$–1.25) separating from the cylinder, and an enlarged view of the vortices near the downstream edge of the photographs (figures 16a_1, 16b_1, 16c_1, 16d_1). Vortices in the wake appear relatively strong in Category *D* and weak in Category *E* (figures *a*(i), *b*(i), *c*(i), *d*(i)). The K-H vortices (figures *a*(ii), *b*(ii), *c*(ii), *d*(ii)) in Category *D* are relatively larger in size and lower in frequency than in other categories. Furthermore, the Kármán vortex

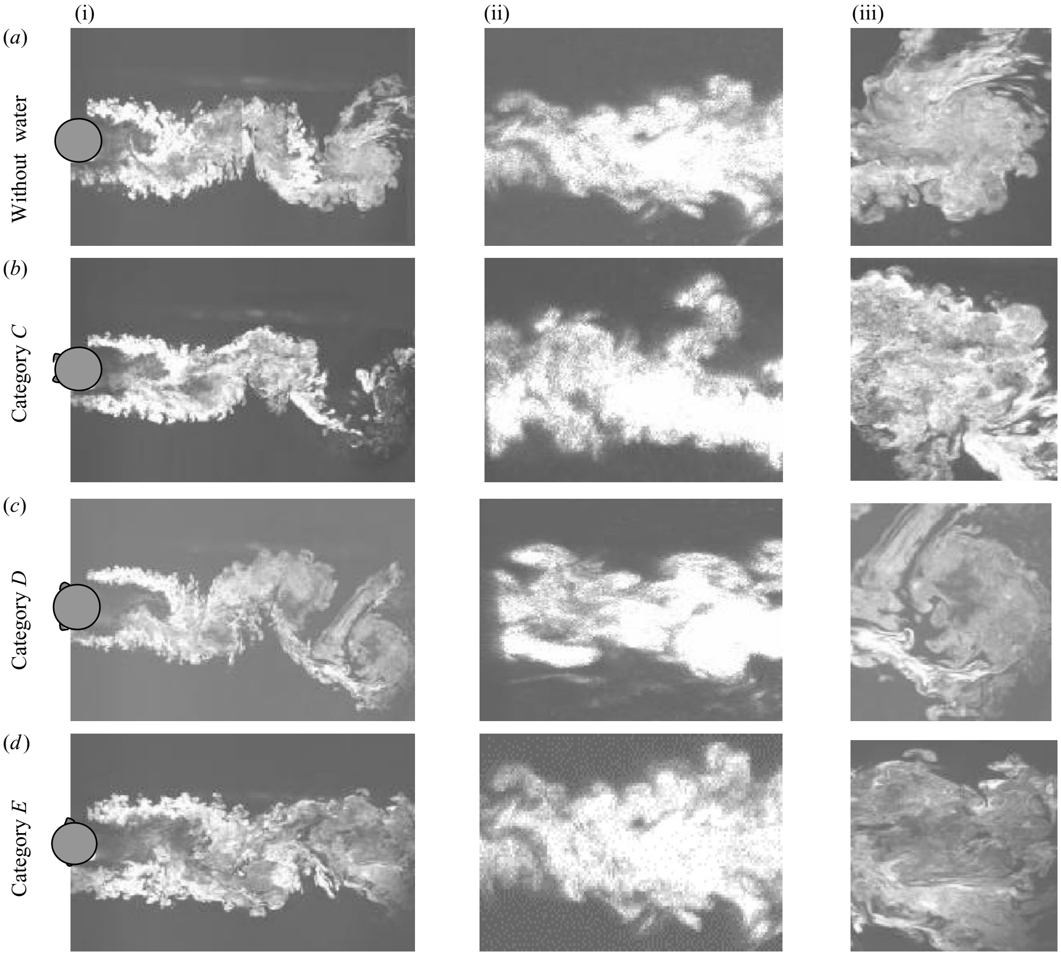

FIGURE 16. Smoke flow visualization at $\alpha = 80^\circ$: (*a*)(i) without water ($Re = 6800$); (*b*)(i) Category *C* ($Re = 3800$); (*c*)(i) Category *D* ($Re = 6800$); (*d*)(i) Category *E* ($Re = 11\,200$); $x^* = -0.25$–8.75, $y^* = 2.5$–2.5. (ii) The magnified photographs, about 8 times, of region $x^* = 0$–1, $y^* = 0.5$– 1.25; they show the small-scale Kelvin–Helmholtz vortices in the separating shear layer. (iii) The magnified photographs, about twice, of the vortex near the downstream edge of the photographs.

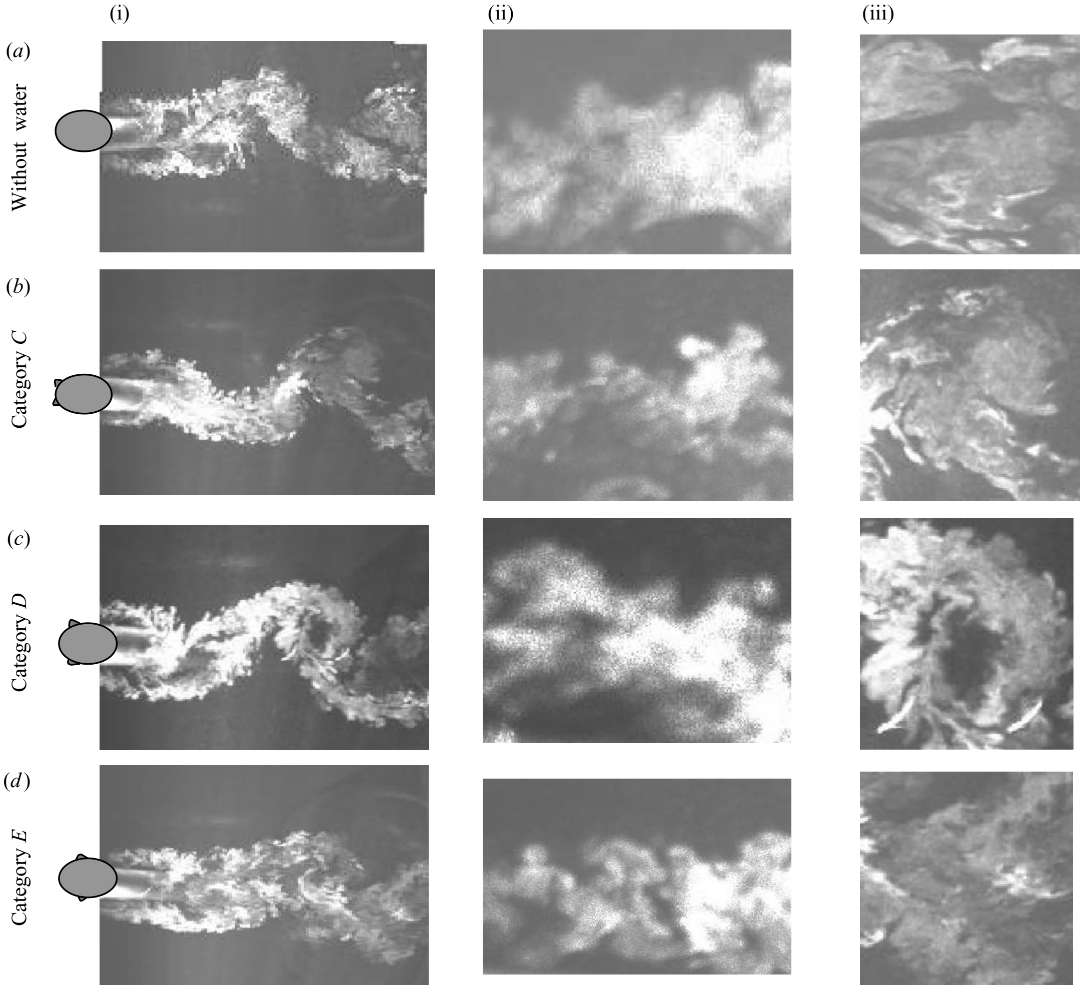

FIGURE 17. Smoke flow visualization at $\alpha = 55^\circ$: (*a*)(i) without water ($Re = 9600$); (*b*)(i) Category *C* ($Re = 5200$), (*c*)(i) Category *D* ($Re = 9600$), (*d*)(i) Category *E* ($Re = 15\,000$); $x^* = -0.25$–7.75, $y^* = 2.5$–2.5. (ii) The magnified photographs, about 8 times, of region $x^* = 0$–1, $y^* = 0.5$–1.25; they show the small-scale Kelvin–Helmholtz vortices in the separating shear layer. (iii) The magnified photographs, about twice, of the vortex near the downstream edge of the photographs.

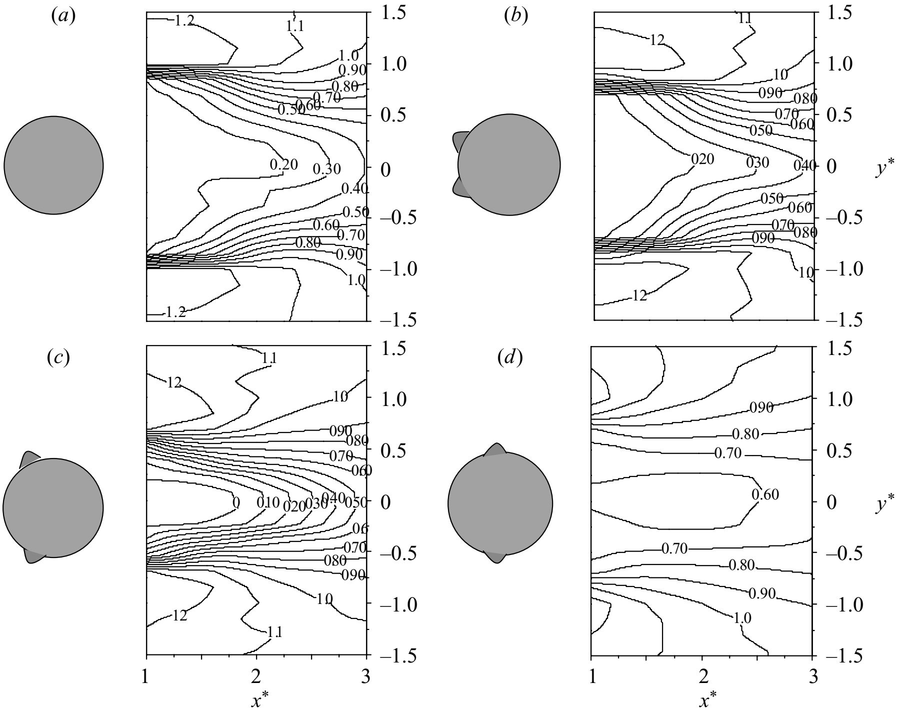

FIGURE 18. Distribution of time-averaged streamwise velocity $\overline{U}^*$ in the (x, y)-plane at $\alpha = 80°$: (*a*) Re =6800, without water; (*b*) Category *C* (Re = 4900); (*c*) Category *D* (Re = 6800); (*d*) Category *E* (Re = 11 200).

(figure *c*(ii)) in Category *D* appears best organized, forming a clear vortex eye, which indicates an improved two-dimensionality. It is proposed that the relatively large quasi-periodic oscillation of the water rivulet in Category *D* induces K-H vortices of large size and low frequency, which feed into Kármán vortices and contribute to their higher strength and lower frequency (figures 12 to 15) than other flow categories.

5.2.2. *Streamwise velocity and vortex formation length*

Since the flow around and forces on the cylinder are closely linked with each other, it is crucial to examine the flow field in order to understand the observations made in §4 and gain insight into the physics associated with the RWI vibration. Figures 18 to 21 present the iso-contours of the LDA-measured time-averaged and r.m.s. streamwise velocities, $\overline{U}^*$ and u^*_{rms}, at $x^* = 1$, 1.5, 2 and 3 ($y^* = -4$–4) for Categories *C*, *D* and *E*. Categories *A* and *B* are expected to be similar to the cases without water and thus were not measured. The case in the absence of water rivulets (figures 18*a*, 19*a*, 20*a*, 21*a*) serves as a reference to evaluate the effect of the rivulets.

Evidently, the rivulets and their positions have a significant impact on the near wake. Noting that the increment of the contours is identical in figures 18 and 19, the contours along the centreline are most densely distributed in Category *D* (figures 18*c*, 19*c*), implying a larger velocity gradient $\partial\overline{U}^*/\partial x$ or a faster recovery of velocity deficit $(1 - \overline{U}^*)$ than in the other categories. This also suggests strong vortex shedding and strong entrainment of fluid from the free stream into the wake (to be confirmed later). For $x^* < 2.0$ at $\alpha = 80°$ (figure 18) and $x^* < 1.5$ at $\alpha = 55°$ (figure 19), $\overline{U}^*$ is smaller in

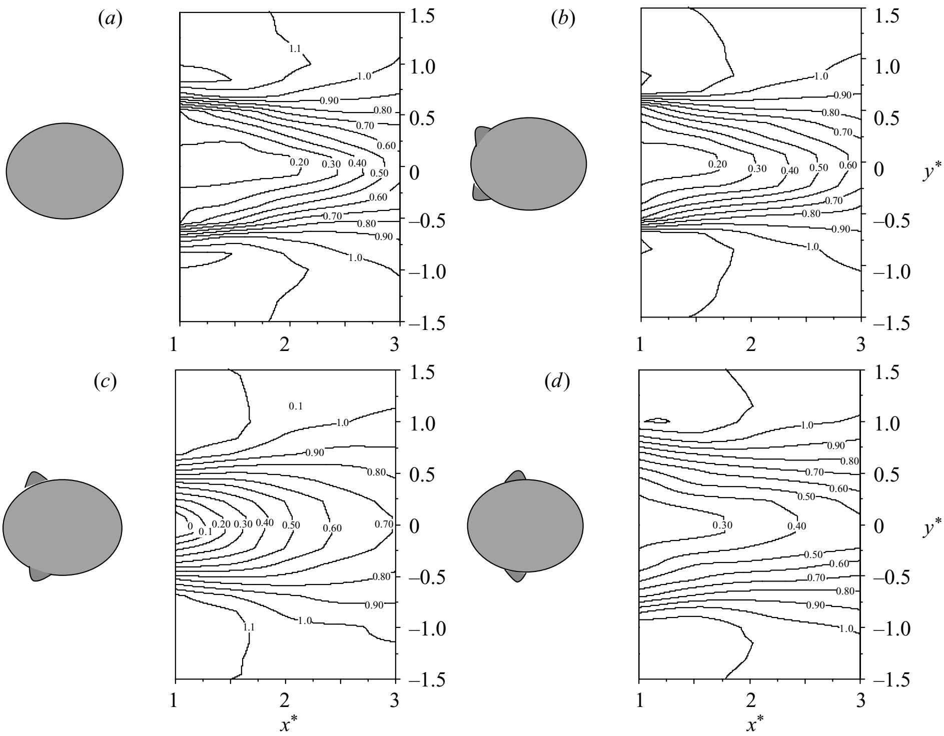

FIGURE 19. Distribution of time-averaged streamwise velocity $\overline{U}^*$ in the (x, y)-plane at $\alpha = 55°$: (*a*) $Re = 9600$, without water; (*b*) Category C ($Re = 6660$); (*c*) Category D ($Re = 9600$); (*d*) Category E ($Re = 15\,000$).

Category D than in the other categories. This observation is consistent with the large mean drag in this category. However, because of a higher velocity deficit recovery, $\overline{U}^*$ becomes larger in Category D than in other categories for $x^* > 2.0$ at $\alpha = 80°$ or $x^* > 1.5$ at $\alpha = 55°$.

The measured maximum u^*_{rms} is 0.36, 0.40, 0.52 and 0.32 at $\alpha = 80°$ (figure 20) in the absence of water ($Re = 6800$), Categories C ($Re = 4900$), D ($Re = 6800$) and E ($Re = 11\,200$), respectively; the corresponding u^*_{rms} is 0.38, 0.39, 0.45 and 0.31 at $\alpha = 55°$ (figure 21). There is a small difference in the maximum u^*_{rms}, as well as in the centreline mean velocity deficit, $1 - \overline{U}^*$ (figures 18*b*, 19*b*), between Category C (figures 20*b* and 21*b*) and those without water (figures 18*a*, 19*a*, 20*a* and 21*a*), which is consistent with the earlier observation that the effect of water rivulets on forces is insignificant in Category C. Apparently, the maximum u^*_{rms} in Category D is markedly higher than that in the other categories, reconfirming much stronger vortex shedding in this category. Category E is characterized by weak u^*_{rms} (figures 20*d* and 21*d*), even smaller than that in the absence of water (cf. figures 20*a* and 21*a*), indicating impaired vortices, consistent with spectral analysis (figures 12*d*, *j* and 13*d*, *j*) and the measured forces (figures 7 and 9). The u^*_{rms}-contours are highly concentrated in the vortex formation region in Category D (figures 20*c* and 21*c*), and decays downstream more rapidly than in the other categories, which may be inferred from the densely distributed contours near the peak.

Following Bloor (1964), the vortex formation length is defined as the distance between the cylinder axis and the location where the streamwise fluctuating velocity

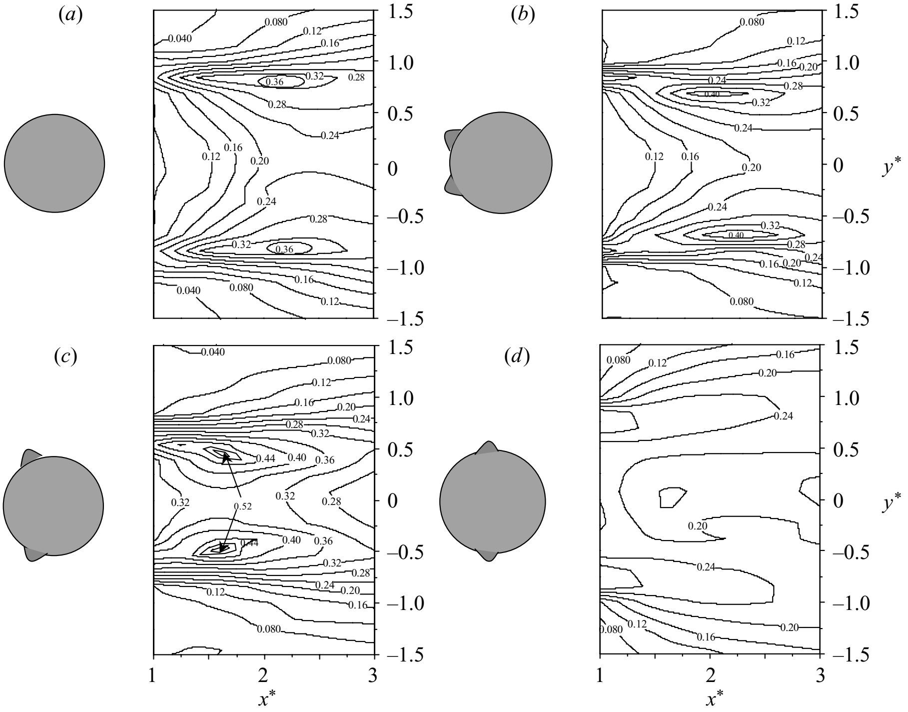

FIGURE 20. Distribution of the fluctuating streamwise velocity u^*_{rms} in the (x, y)-plane at $\alpha = 80°$: (*a*) $Re = 6800$, without water; (*b*) Category *C* ($Re = 4900$); (*c*) Category *D* ($Re = 6800$); (*d*) Category *E* ($Re = 11\,200$).

reaches the maximum. This length is a parameter that may significantly influence C_D, C'_D and C'_L; a short length corresponds to higher C_D, C'_D and C'_L or vice versa (Bloor 1964; Griffin 1971; Zdravkovich 1997). Figure 20 shows that the maximum u_{rms} at $\alpha = 80°$ occurs approximately at $(x^*, y^*) = (2.2, \pm 0.9)$, $(2.2, \pm 0.75)$, $(1.65, \pm 0.5)$ and $(2, \pm 0.75)$ for the absence of water (figure 20*a*), Categories *C* (figure 20*b*), *D* (figure 20*c*) and *E* (figure 20*d*), respectively. Similarly, figure 21 shows that the maximum u^*_{rms} at $\alpha = 55°$ occurs approximately at $(x^*, y^*) = (2.0, \pm 0.55)$, $(1.8, \pm 0.5)$, $(1.45, \pm 0.45)$ and $(2.0, \pm 0.63)$ for the absence of water (figure 21*a*), Categories *C* (figure 21*b*), *D* (figure 21*c*) and *E* (figure 21*d*), respectively. In Category *D*, the vortex formation length retreats markedly, changing from $x^* = 2.2$ at $\alpha = 80°$ and 2.0 at $\alpha = 55°$ (without water) to 1.65 and 1.45, respectively. The observation bears a strong resemblance to the so-called lock-on phenomenon, where the frequency of vortex shedding from a cylinder is modified to synchronize with an externally forced vibration.Griffin & Ramberg (1974) observed that at $Re = 190$, as the forced oscillation amplitude increased from zero to $0.5d$, the lock-on occurred, resulting in a decrease in the vortex formation length by $1d$. A similar observation was made by Krishnamoorthy, Price & Paidoussis (2001) at $Re \approx 1500$. Griffin & Ramberg further noted an inverse relationship between the vortex strength and the vortex formation length.

It is worth commenting on the wake width. This parameter, defined as the transverse distance between the free shear layers in the wake (e.g. Roshko 1954; Balachandar, Mittal & Najjar 1997), characterizes the wake and has a great influence on forces on a body. This width may also be defined as the transverse distance between the

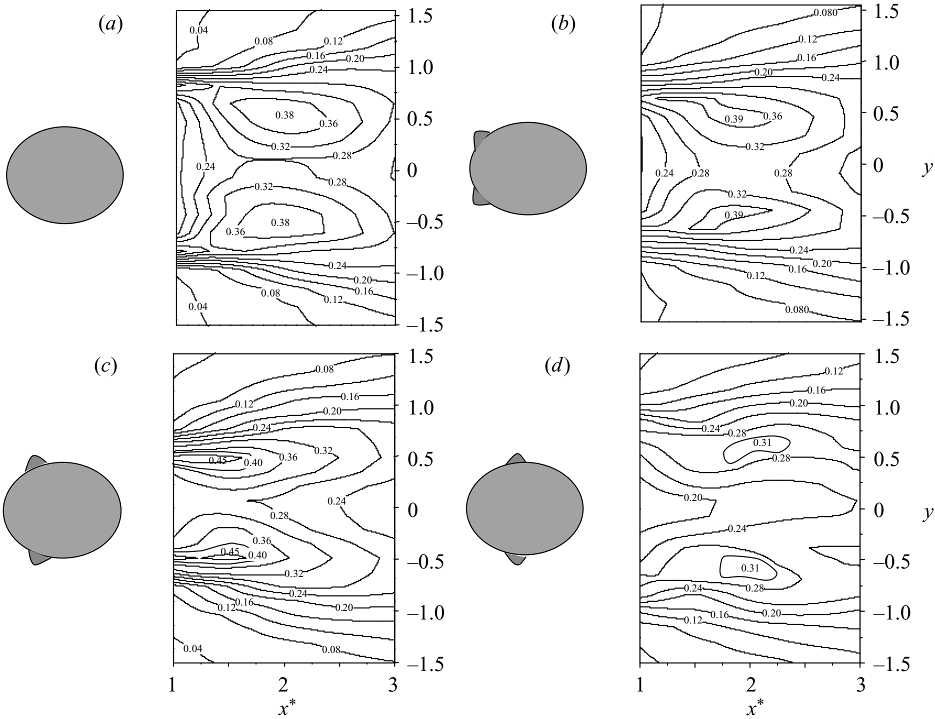

FIGURE 21. Distribution of the fluctuating streamwise velocity u^*_{rms} in the (x, y)-plane at $\alpha = 55°$: (a) $Re = 9600$, without water; (b) Category C ($Re = 6660$); (c) Category D ($Re = 9600$); (d) Category E ($Re = 15\,000$).

two maximum u^*_{rms} in the iso-contours of u^*_{rms} (Griffin & Ramberg 1974; Ramberg 1983). As such, the wake width shrinks markedly in Category D, changing from 1.8d without water to 1.0d with water at $\alpha = 80°$ or 1.1d to 0.9d at $\alpha = 55°$ (figures 20a, c, and 21a, c).

The wake width could also be inferred from $\overline{U}^*$ (figures 18 and 19). The gradient $\partial \overline{U}^* / \partial y^*$ (figure 22) at $x^* = 1.5$ and 2.0, which are very close to the streamwise location of the maximum u^*_{rms} (figure 20), displays two pronounced peaks, one positive and the other negative, at $y^* = \pm 0.86$, ± 0.72, ± 0.47 and ± 0.68 for the case without water ($Re = 6800$) and those with water ($Re = 4900$, 6800 and 11 200), respectively. The two peaks coincide approximately with the lateral position of the corresponding maximum u^*_{rms} (figure 20). Evidently, the peaks become less pronounced and broader with increasing x^*.

5.2.3. *Cross-stream velocity and fluctuation*

Time-averaged and fluctuating lateral velocities, $\overline{V}^*$ and v^*_{rms}, provide a measure of the entrainment of ambient fluid into the wake, and also the information on the vortex formation and forces on the cylinder. Figures 23 and 24 present $\overline{V}^*$ and v^*_{rms} for $\alpha = 80°$, measured using laser-Doppler anemometry (LDA) for Categories C, D and E with and without water rivulets. The results at $\alpha = 55°$ show essentially the same trend as at $\alpha = 80°$ and therefore are not presented. In each case, $\overline{V}^*$ (figure 23) displays a twin peak, one on each side of the centreline, and v^*_{rms} (figure 24) shows a single peak on the centreline. The maximum magnitude of $\overline{V}^*$ is 0.21, 0.22, 0.25 and

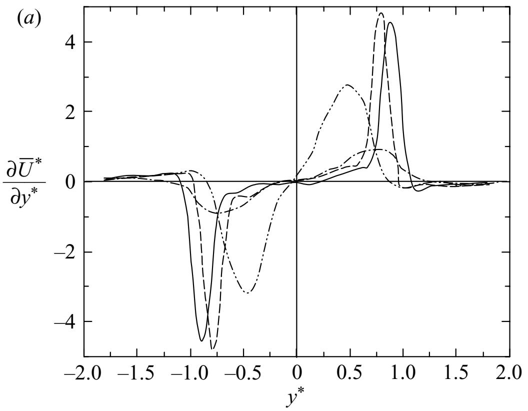

FIGURE 22. The u-component velocity gradient in the lateral direction at $\alpha = 80°$: (a) $x^* = 1.5$, (b) 2.0. ——, $Re = 6800$, without water; — — —, 4900, with water; —·· — ··—, 6800, with water; —· — ·—, 11200, with water.

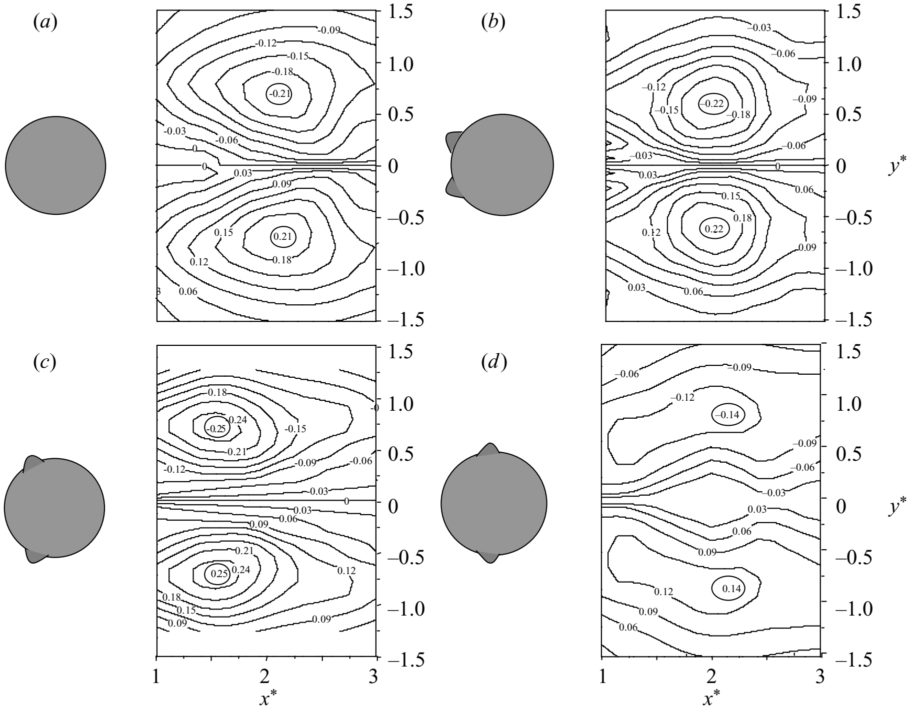

FIGURE 23. Distribution of time-averaged lateral $\overline{V}^*$ velocity in the (x, y)-plane at $\alpha = 80°$: (a) $Re = 6800$, without water; (b) Category C ($Re = 4900$); (c) Category D ($Re = 6800$); (d) Category E ($Re = 11\,200$).

0.14 for the absence of water, Categories C, D and E, respectively. This magnitude is largest in Category D and smallest in E, implying large and small entrainments, respectively.

In contrast with the u^*_{rms} contours, the v^*_{rms} contours (figure 24) show one maximum only. This maximum occurs at $x^* = 1.8$ for $\alpha = 80°$ in Category D, which is the

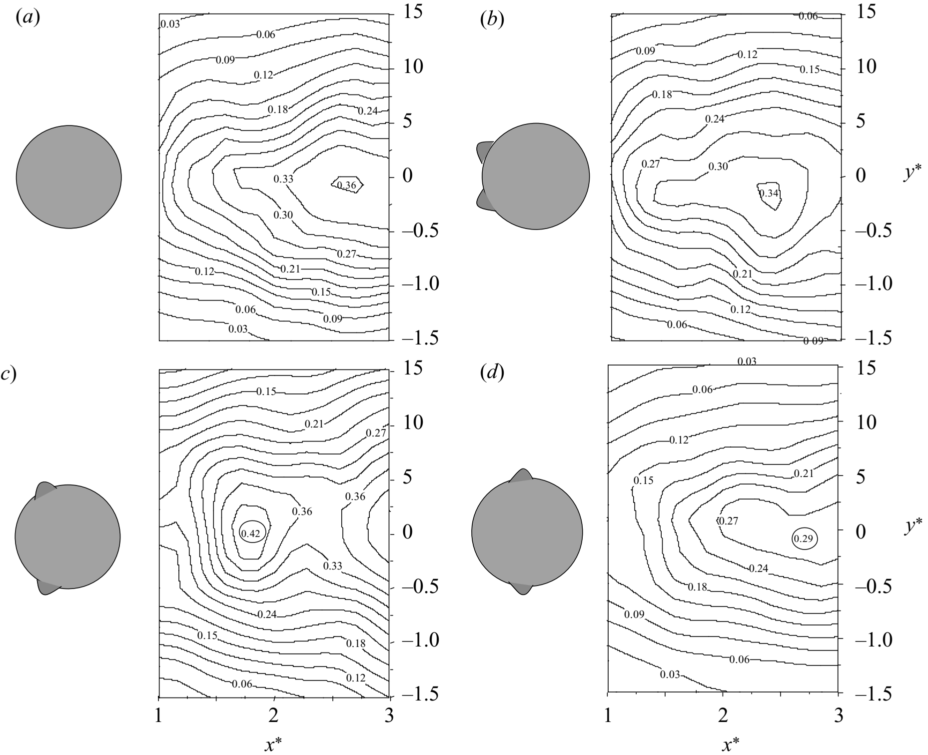

FIGURE 24. Distribution of the fluctuating lateral velocity v^*_{rms} in the (x, y)-plane at $\alpha = 80°$: (a) $Re = 6800$, without water; (b) Category C ($Re = 4900$); (c) Category D ($Re = 6800$); (d) Category E ($Re = 11\,200$).

nearest to the cylinder of all the cases. The occurrence of the maximum v^*_{rms} is further downstream of that in the $\overline{V}^*$ (figure 23) or u^*_{rms} (figure 20) contours, similarly to the case of $\alpha = 90°$. Balachandar *et al.* (1997) examined the u_{rms} and v_{rms} contours in the wake of a circular cylinder normal to incident flow and noted the maximum u_{rms} at $x^* = 0.85$ and the maximum v_{rms} at $x^* = 1.2$ for $Re = 300$. Sung & Yoo (2003) reported the maximum u_{rms} and v_{rms} at $x^* = 0.75$ and 1.7, respectively, for $Re = 360$. Paranthoen *et al.* (1999) observed the maximum u_{rms} and v_{rms} at $x^* = 5$ and 7, respectively, for $Re = 53.3$.

5.2.4. *The z-component velocity and flow three-dimensionality*

The time-averaged velocity $\overline{W}$, normal to $\overline{U}$ and $\overline{V}$, may provide a measure of the flow three-dimensionality. A large $\overline{W}$ corresponds to a high degree of three-dimensionality. In the wake of a cylinder placed normal to incident flow, $\overline{W}$ should be approximately zero. The same may not be true when the cylinder is inclined; the W-component of the velocity in the wake of an inclined cylinder is an important parameter, as the flow is by nature three-dimensional (Ramberg 1983).

Figure 25 presents LDA-measured $\overline{W}^*$ at $x^* = 1$–2 with and without running water rivulets. In the absence of water rivulets, $\overline{W}^*$ (figure 25a, c) is positive for $y^* < 0.85$ at $\alpha = 80°$ and for $y^* < 0.65$ at $\alpha = 55°$, and negative for $y^* > 0.85$ at $\alpha = 80°$ and for $y^* > 0.65$ at $\alpha = 55°$. $\overline{W}^*$ has a large gradient near $y^* = 0.85$ for $\alpha = 80°$ and $y^* = 0.65$ for $\alpha = 55°$ along the y-direction, implying strong streamwise vorticity

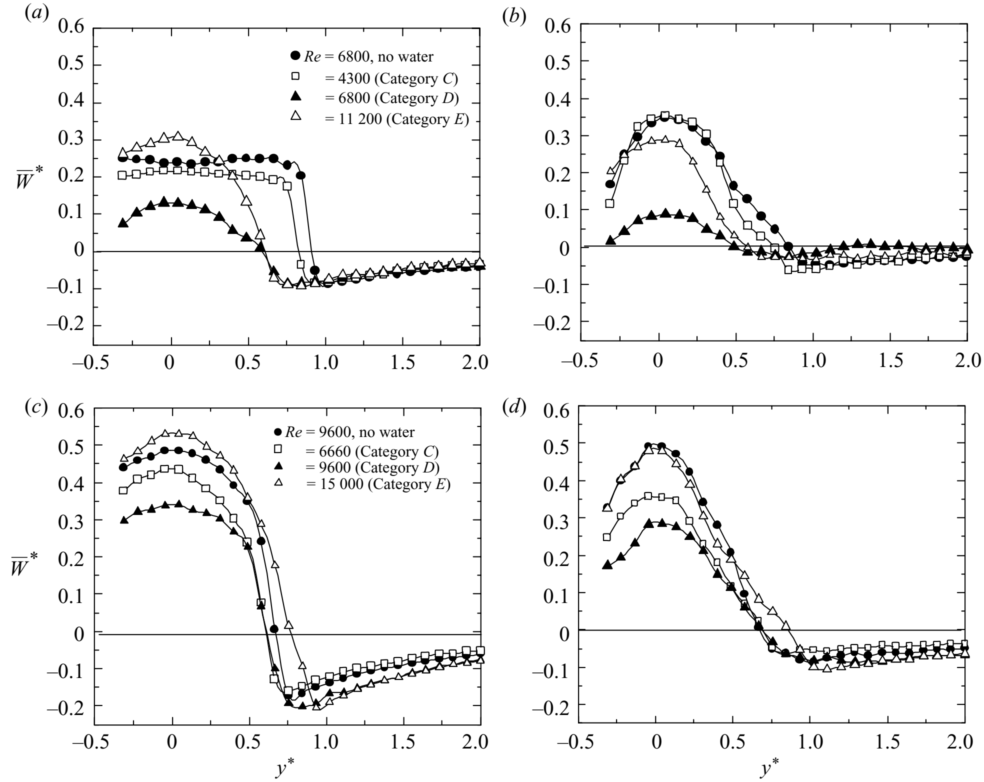

FIGURE 25. Distribution of time-averaged z-component velocity $\overline{W}^*$ across the wake at (a) $x^* = 1.0$, $\alpha = 80°$; (b) 2.0, 80°; (c) 1.0, 55°; (d) 2.0, 55°.

$\omega_x (\equiv \partial V/\partial z - \partial W/\partial y)$. A scenario is proposed in figure 26 in order to understand thoroughly such a large gradient in $\overline{W}^*$ or large ω_x. U_∞ may be decomposed into two components, i.e. u_x and u_z along the x'- and z'-directions, respectively. Assuming a frictionless cylinder surface in an idealized case, $u_{z'}$ should be uniform (figure 26a) and the resultant velocity behind the cylinder remains along the x-direction, with a zero component ($W = 0$) along the z-direction. In reality, a boundary layer is developed around the cylinder surface owing to friction between the axial flow $u_{z'}$ and the surface. As such, W would be positive in the inner layer of the boundary layer because of a decrease in $u_{z'}$ near the cylinder surface, and negative in the outer layer because of an increase in $u_{z'}$ (figure 26b). The scenario is consistent with the $\overline{W}^*$ distribution (figure 25) in the absence of the rivulets; $\overline{W}^*$ is positive near the centreline, say at $y^* < 0.8$ in figure 25a, and negative at large y^* (>0.8 in figure 25a).

The magnitude of $\overline{W}^*$, irrespective of its sign, is considerably larger at $\alpha = 55°$ than at $\alpha = 80°$, producing a larger $\partial \overline{W}^*/\partial y$ between the positive or negative $\overline{W}^*$ and subsequently a larger ω_x at $\alpha = 55°$. In other words, the two-dimensionality of the wake deteriorates from $\alpha = 80°$ to 55°. $\overline{W}^*$ exhibits a substantial reduction in magnitude near the centreline ($\overline{W}^* > 0$) and away from the centreline ($\overline{W}^* < 0$) in Category C ($Re = 4300$ for $\alpha = 80°$; 6660 for $\alpha = 55°$) and in Category D ($Re = 6800$ for $\alpha = 80°$; 9600 for $\alpha = 55°$). As indicated in figure 26(b), if a running water rivulet occurs on the vortex-generating surface (on which the flow is attached) of the cylinder, $u_{z'}$ would be increased, compared with that without water, near the surface owing

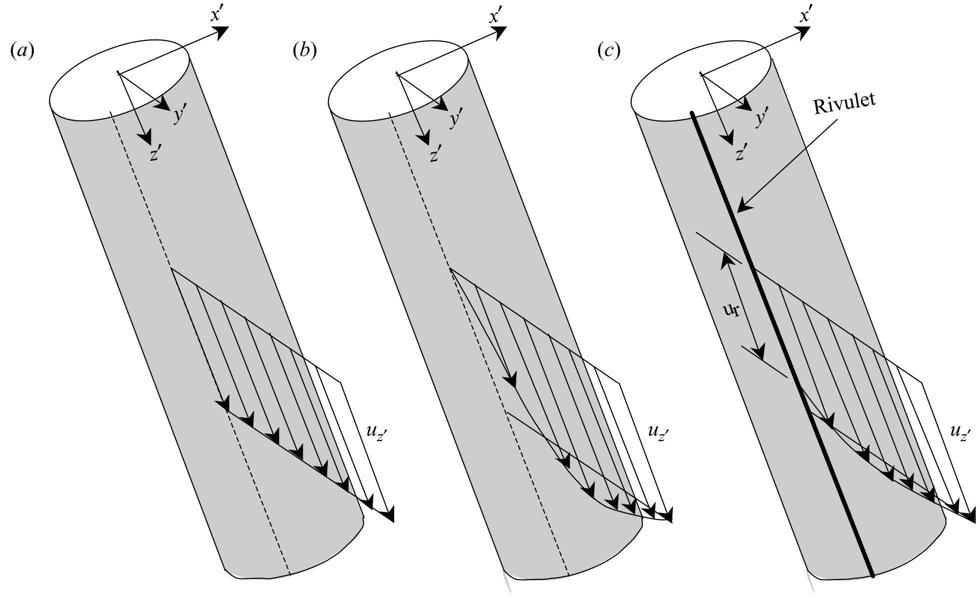

FIGURE 26. Axial flow velocity distribution on (*a*) frictionless surface, (*b*) frictional surface without water, and (*c*) frictional surface with water. Where u_r is the axial velocity of water rivulet.

to the velocity of water (figure 26*c*), resulting in lower $\partial u_{z'}/\partial y$ and subsequently a smaller $\partial \overline{W}^*/\partial y$ or ω_x. Note that the greatest reduction in $\overline{W}^*$ occurs in Category *D*. Evidently, the running water rivulets in this category, when forcing the boundary layers to separate early, enhance the flow two-dimensionality and hence the fluctuating forces on the cylinder. On the other hand, in Category *E* ($Re = 11\,200$ for $\alpha = 80°$; $13\,900$ for $\alpha = 55°$) where the rivulets occur behind the separation line, $\overline{W}^*$ around $y^* = 0$ is slightly higher at $x^* = 1.0$ but lower at $x^* = 2.0$ with water than without water. The reason for this is not clear.

In order to substantiate further the proposed scenario for the variation in $\overline{W}^*$, the water flow rate, *Q*, was increased by 20 %, from 25 to 30 l h^{-1} (corresponding to Re_w of about 32 and 39, respectively), and the maximum magnitude of $\overline{W}^*$ was observed to reduce by about 16–19 % (figure 27), regardless of the αvalue, confirming that the running water rivulets do enhance the flow two-dimensionality. It may be concluded that the RWI vibration could be at least partially ascribed to the fact that the running water rivulets lead to an improved two-dimensionality of the flow around the cylinder.

It is interesting to examine the influence of *Q* or Re_w on the quantitative vorticity data, which is directly linked to forces on the cylinder. The ω_z^* contours at $Re_w = 32$ are compared with those at $Re_w = 39$ for Category *D* (figure 28). Because of an increase in Re_w from 32 to 39, the maximum ω_z^* grows by about 10 %. A higher Re_w implies a higher momentum of water passing through a rivulet section and a higher loss of potential energy (due to gravity) of water for a given length of water rivulet. Two factors contribute to the loss of energy, i.e. the viscous loss due to friction between cylinder surface and running water, and the energy exchange from water to air due to friction between water and air. As demonstrated earlier, running water increases the z'-component of air velocity, implying a gain of momentum by air and hence a contribution to the energy increase in the wake. Therefore, a higher Re_w

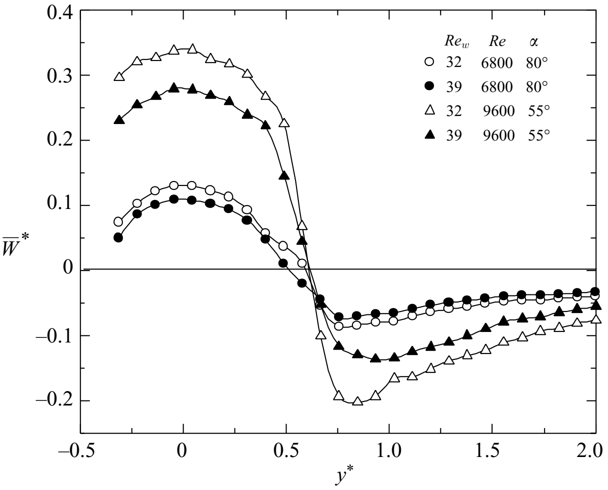

FIGURE 27. Effect of water flow rate on $\overline{W}^*$ across the wake at $x^* = 1.0$.

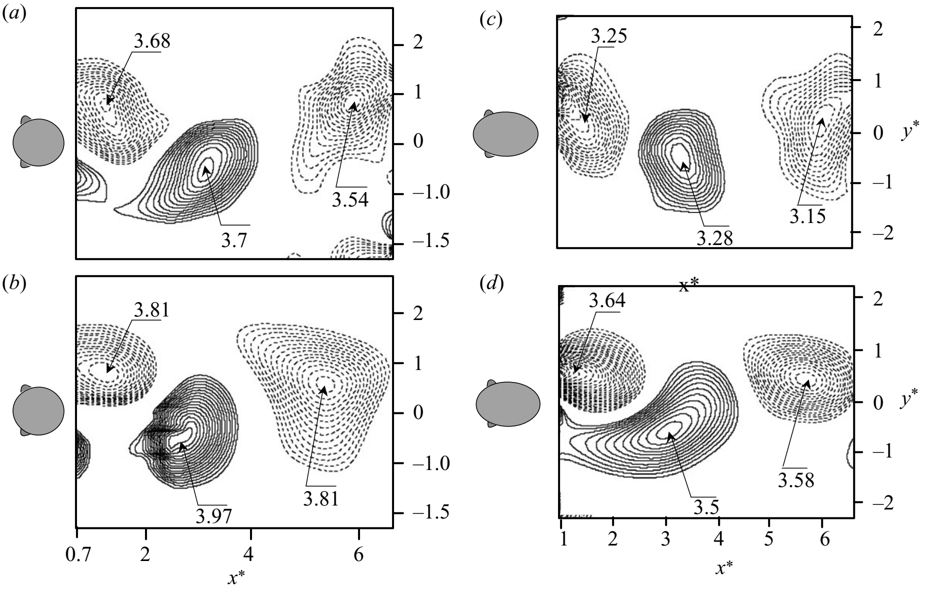

FIGURE 28. Effect of Q on instantaneous vorticity contours $\omega_z^* = \omega_z d/U_\infty$ at Category D: (*a*) $Q = 25\,\mathrm{l\,h^{-1}}$ ($Re_w = 32$), $\alpha = 80°$; (*b*) $Q = 30\,\mathrm{l\,h^{-1}}$ ($Re_w = 39$), $\alpha = 80°$; (*c*) $Q = 25\,\mathrm{l\,h^{-1}}$ $(Re)_w = 32$), $\alpha = 55°$; (*d*) $Q = 30\,\mathrm{l\,h^{-1}}$ ($Re_w = 39$), $\alpha = 55°$. ——, positive and - - -, negative vorticity contours. The level of the outer contour is about 80 % of the maximum ω_z^*.

provides a higher energy transfer from water to air, contributing to the improved flow two-dimensionality, the increased vorticity strength and forces, etc.

The above discussion reaffirms that running water rivulets play an important role in the near-wake fluid dynamics and their effect differs from that of stationary or oscillating artificial rivulets. The result corroborates Flamand's (1995) and Verwiebe & Ruscheweyh's (1998) propositions that a natural rivulet could not be modelled by a stationary rivulet since the natural rivulet is running along the cylinder as well as oscillating circumferentially, both having a profound influence on the RWI vibrations.

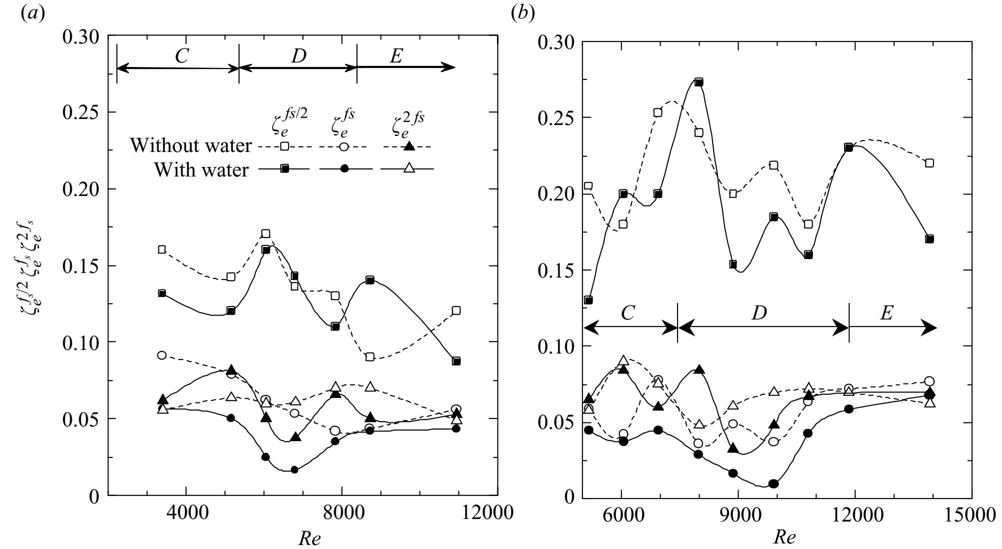

FIGURE 29. Effective damping ratios: $\zeta_e^{f_s/2}$ at $f_s/2$, $\zeta_e^{f_s}$ at f_s, $\zeta_e^{2f_s}$ at $2f_s$, (*a*) $\alpha = 80°$, (*b*) $\alpha = 55°$.

6. Discussion

Before a discussion of the mechanisms of the RWI vibration, it is useful to examine how the effective damping of the fluid–cylinder system varies with *Re*. Damping is a parameter that characterizes the fluid–structure instability. The effective damping consists of both structural and fluid damping. A violent structural vibration is often associated with negative fluid or low effective damping, which may occur because of the lock-in of f_s with the natural frequency of the fluid–structure system (Zhou *et al.* 2001). Zhang et al. (2003) used the auto-regressive moving average (ARMA) technique developed by Mignolet & Red-Horse (1994) to deduce effective damping ratios (including structural and fluid damping) from the measured strain on a free-vibrating cylinder in cross-flow. The same technique was used here to calculate, from the lift signals, effective damping ratios, $\zeta_e^{f_s/2}$, $\zeta_e^{f_s}$ and $\zeta_e^{2f_s}$, at $f_s/2$ (the nearest sub-harmonic), f_s and $2f_s$ (the nearest super-harmonic), respectively (figure 29). In general, $\zeta_e^{f_s}$ and $\zeta_e^{2f_s}$ are comparable and much smaller than $\zeta_e^{f_s/2}$. $\zeta_e^{f_s}$ displays a significant dip in Category *D*, reaching the minimum 0.015 at $Re = 6800$ for $\alpha = 80°$ and 0.01 at $Re = 9600$ for $\alpha = 55°$, where the fluid forces on the cylinder were at a maximum. The minima are very small compared with that in other categories or in the absence of water, suggesting the possible occurrence of the 'lock-in' phenomenon. The vortex-shedding frequency in the present measurement conditions was less than 85 Hz, while the natural frequency of the fluid–structure system was about 127 Hz, thus excluding the possibility of lock-in between vortex shedding and the natural frequency of the fluid–structure system.

When the lock-in occurs with a forced vibrating cylinder in cross-flow, C_L' increases (Bishop & Hassan 1964; Taneda & Honji 1967; Protos, Goldschmidt & Toebes 1968). So does C_D (Tanida, Okajima & Watanabe 1973). Zdravkovich (1982) concluded that the main feature of vortex shedding synchronizing with an oscillating cylinder was to magnify greatly C_D' and C_L', compared with a stationary cylinder. A number of factors contribute to this magnification associated with the lock-in phenomenon, including the reduced vortex formation length (Gerrard 1966; Griffin & Votaw 1972), the prolonged spanwise correlation length (Toebes 1969) and the increased period of vortex shedding (Sarpkaya 1979). The lock-in is in general characterized by (i) the synchronization of the cylinder oscillation with fluctuating lift and vortex shedding from the cylinder (Bishop & Hassan 1964; Govardhan & Williamson 2000), (ii) a short vortex formation region (Griffin 1971; Govardhan & Williamson 2001), (iii) a reduced wake width, (iv) the increased C_D, C_D' and C_L' (Govardhan & Williamson 2000; Carberry, Sheridan & Rockwell 2001), Okamoto, Uematsu & Taguwa 2002; Guilmineau & Queutey 2004), (v) a conspicuous increase in the spanwise correlation length of fluctuating velocity or pressure, i.e. an improved two-dimensionality of flow around the cylinder (Hover, Tredt & Triantafyllou 1998), (vi) a considerable increase in the vortex strength (Gu, Chyu & Rockwell 1994) or fluctuating velocities (Govardhan & Williamson 2001), (vii) an increase in the oscillation of the separation points (Sarpkaya, 1979), and (viii) a low effective damping ratio, i.e. the sum of fluid and structural damping ratios (Zhou *et al.* 2001).

Category *D* exhibits almost all the characteristics of the lock-in phenomenon. (i) Vortex shedding and fluctuating lift are correlated much better than in other categories as well as in the absence of water (figure 13). (ii) The vortex formation length is substantially shorter (figures 20 and 21) than in the other cases. (iii) The two-dimensionality of the flow in the wake is improved (figure 25). (iv) There is a significant increase in the vortex strength (figures 14, 15) and in u^*_{rms} and v^*_{rms} (figures 20, 21 and 24). (v) The significant water rivulet oscillation points to the increased oscillation of the flow separation point given an association between flow separation and water rivulet oscillation. (vi) *St* is reduced considerably. (vii) A low effective damping ratio (figure 29) is observed. Finally, C_D, C_D' and C_L' are greatly augmented (figures 7 and 9). This naturally begs the question why Category *D* is so similar to the flow associated with the lock-in phenomenon in a forced vibrating cylinder in cross-flow.

Using an optical technique, Lemaitre (2006) showed experimentally that the rivulets oscillated at the same frequency as Kármán vortex shedding. She estimated the fundamental frequency of rivulet oscillation using the Rayleigh method and obtained good agreement with her measurements. A theoretical model was developed based on the Vander Pol equation, which connected the lowest capillary mode of the rivulets with the flow around the cylinder. The solution to this equation suggested a lock-in of the vortex-shedding frequency with the rivulet eigen-frequency for a certain range of wind speed. In this range of wind speed, a strong amplification of fluctuating lift was observed, which is consistent with the present proposition of the possible mechanism behind the RWI vibration.

Zhang, Cheng & Zhou (2004) investigated flow control based on a perturbation, generated by piezoelectric ceramic actuators, on one surface of a flexibly supported square cylinder in cross-flow. They found that, under the resonance condition when vortex shedding from the cylinder was in synchronization with the natural frequency of the fluid–structure system, a very small surface perturbation (only 0.6 % of the cylinder height) could double the vortex strength and reduce significantly the fluid–structure system damping as long as the perturbation was made in phase with vortex shedding or the natural frequency of the fluid–structure system through a feedback control system. Subsequently, the cylinder oscillating amplitude was greatly amplified.

A mechanism, referred to as a rivulet-vortex-induced vibration (RVIV), is proposed for the RWI cable vibration. Under interactions between rain and wind, two running rivulets are formed along the cable. At the correct range of wind speed, which depends on the rate of water flow along the cable, the inclination and yaw angles of the cable, the rivulets may approach the flow separation line and hence oscillate circumferentially when interacting with flow separation. They act effectively to perturb or impose a perturbation force on flow separation. When the flow separation frequency coincides with the natural frequency (or its harmonics) of the circumferentially oscillating rivulets, they synchronize with each other. Given that the two synchronized frequencies approach the natural frequency of the fluid–cable system (or its harmonics), the rivulet oscillation, flow separation and cable vibration could all be 'locked-in' with each other. This proposition is consistent with Cosentino *et al.*'s (2003*a*) observation that the rivulet oscillation frequency was identical to the sub-harmonic of the vortex-shedding frequency when the vortex-shedding frequency and the cable vibration were in synchronization. In view of the great impact of a small perturbation on fluid–structure interactions (Zhang *et al.* 2004), it seems plausible that the rivulet oscillation plays a key role in the RVIV, and could have a profound effect on the RWI vibration. The 'lock-in' of the three dynamic processes could greatly enhance vortex shedding and reduce the fluid–cable system damping. As a consequence, the excitation force and hence the cable vibrating amplitude may be greatly amplified.

Note that the cylinder in the present measurement was rigid and fix-supported, implying a large damping and negligibly small vibration. Although vortex shedding and rivulet oscillation may have been locked in with each other, they cannot be synchronized with the natural frequency of the fluid–tructure system. Thus, the running water rivulets could have only a limited effect on the vortex-shedding strength, fluctuating forces, effective damping, etc. The vibration of the cylinder may have a significant effect on the formation of the rivulets, and a much more complex dynamics will be involved in the vibrating system. For example, the rivulets may effectively produce a roughness on the cylinder. The roughness (protuberance) of a vibrating circular cylinder may suppress or enhance flow-induced vibration, depending on the location of the roughness. In their investigation of the effects of tripping wires on the vortex excitation of a circular cylinder, Hover *et al.* (2001) placed two 0.23 mm diameter tripping wires at 70° from the mean stagnation point of a 76.2 mm diameter cylinder, resulting in an impaired vibration. Sangil & Sakamoto (2006*a*) placed tripping wires of 6 mm diameter on a 66 mm diameter cylinder at 40° from the mean stagnation point, suppressing completely the vortex excited cylinder vibration. However, once the tripping wires were placed at 42°–70° (Sangil & Sakamoto 2006*b*), the boundary layer separated from them, generating a large-amplitude cylinder-vibration.

7. Conclusions

Fluid dynamics associated with an inclined stationary cylinder with water running over has been systematically investigated. Two inclination angles, $\alpha = 80^\circ$ and 55°, were examined. Measurements were performed for the formation and behaviours of water rivulets, fluid forces on the cylinder and the near wake. The investigation leads to following conclusions:

1. Flow may be classified into five categories, *A*, *B*, *C*, *D* and *E*, based on the water behaviour on the cylinder surface and associated fluid forces on and flow around the cylinder. Category *A* refers to the case when only one water rivulet forms near the leading stagnation line. *Re* in this category is smaller than 1500 for $\alpha = 80^\circ$ and 3000 for $\alpha = 55^\circ$. In Category *B*, one or two rivulets occur intermittently, corresponding to $Re = 1500$–2500 at $\alpha = 80^\circ$ and 3000–5200 at $\alpha = 55^\circ$. In Category *C*, the two water rivulets occur symmetrically between the leading stagnation and separation lines. The

rivulets should not have any significant effect on flow separation. The Re range is 2500–5300 at $\alpha = 80^\circ$ and 5200–7400 at $\alpha = 55^\circ$. In Category D, the two rivulets move further downstream and force the boundary layers to separate from them, earlier than in the absence of the rivulets. This category corresponds to $Re = 5300$–8400 for $\alpha = 80^\circ$ and $Re = 7400$–$12\,000$ for $\alpha = 55^\circ$. In Category E, the rivulets move just beyond the separation line, with Re exceeding 8400 at $\alpha = 80^\circ$ and 12 000 at $\alpha = 55^\circ$.

2. In Categories A, B and C, the rivulets are steady, without oscillating appreciably, and have limited influence on the fluid forces and the near wake of the cylinder. Category D is distinct from the others. The circumferential oscillation of water rivulets is considerably more significant than in the other flow categories. The near wake is characterized by increased vortex strength, a relatively low Strouhal number, a short vortex formation length and narrow wake, highly correlated vortex shedding and fluctuating lift, a considerably low effective damping ratio, and an improved two-dimensionality of the flow around the cylinder. The maximum C_D' and $C_L{}'$ are about 4.25 and 5.75 times, respectively, their counterparts in the absence of water rivulets for $\alpha = 80^\circ$, and about 4.7 and 2.7 times, respectively, for $\alpha = 55^\circ$. All these bear a close resemblance to the lock-in phenomenon when vortex shedding coincides with the vibration of a cylinder in cross flow, pointing to the lock-in between water rivulet and flow separation. In Category E, the significant oscillation of the rivulets disappears. This category is characterized by weakened vortex shedding and fluctuating velocities, smaller C_D' and $C_L{}'$, less correlated vortex shedding and lift force, and a longer vortex formation length.

3. It is proposed that the rivulet-vortex-induced vibration is one of the causes of the RWI vibration. When the vortex-shedding frequency approaches the natural frequency of the circumferentially oscillating rivulets, they will be locked in with each other. Once the two synchronizing frequencies coincide with the natural frequency of the fluid–cylinder system, all three dynamic processes are ‘locked in’. The occurrence of this ‘lock-in’ is supported by observations made in Category D. As a result, the vortex-shedding strength will be greatly enhanced and the damping of the fluid–structure system could be drastically reduced, leading to violent structural vibration.

4. Water rivulets running along an inclined cable enhance the flow two-dimensionality, which may also contribute to the increased strength of the rivulet-vortex-induced vibration (RVIV).

The work described in this paper was substantially supported by the grant from the Research Grants Council of the Hong Kong Special Administrative Region, China (PolyU 5316/03E). Y. Z. also wishes to acknowledge financial support given to him by France/HK Joint Research Scheme through grant F-HK12/03T. The contribution of Drs Cecile Lemaitre and Pascal Hemon from Ecole Polytechnique, Paris, to the experimental se-tup is gratefully acknowledged.

REFERENCES

Alam, M. M., Moriya, M. & Sakamoto, H. 2003*a* Aerodynamic characteristics of two side-by-side circular cylinders and application of wavelet analysis on the switching phenomenon. *J. Fluids Struct.* **18**, 325–346.

Alam, M. M., Moriya, M., Takai, K. & Sakamoto, H. 2003*b* Fluctuating fluid forces acting on two circular cylinders in a tandem arrangement at a subcritical Reynolds number. *J. Wind Engng Indust. Aerodyn.* **91**, 139–154.

Alam, M. M., Sakamoto, H. & Moriya, M. 2003*c* Reduction of fluid forces acting on a single circular cylinder and two circular cylinders by using tripping rods. *J. Fluids Struct.* **18**, 347–366.

Alam, M. M., Sakamoto, H. & Zhou, Y. 2005 Determination of flow configurations and fluid forces acting on two staggered circular cylinders of equal diameter in cross-flow. *J. Fluids Struct.* **21**, 363–394.

Almosnino, D. & McAlister, K. W. 1984 Water tunnel study of transition flow around circular cylinders. NASA 85879.

Balachandar, S., Mittal, R. & Najjar, F. M. 1997 Properties of the mean recirculation region in the wakes of two-dimensional bluff bodies. *J. Fluid Mech.* **351**, 167–199.

Batham, J. P. 1973 Pressure distribution on circular cylinders at critical Reynolds numbers. *J. Fluid Mech.* **57**, 209–228.

Bearman, P. W. & Trueman, D. M. 1972 An investigation of the flow around rectangular cylinders. *Aero. Q.* **23**, 229–237.

Bishop, R. E. D. & Hassan, A. Y. 1964 The lift and drag forces on a circular cylinder oscillating in a flowing fluid. *Proc. R. Soc. Lond.* A **277**, 51–75.

Bloor, S. M. 1964 The transition to turbulence in the wake of a circular cylinder. *J. Fluid Mech.* **19**, 290–309.

Bosdogianni, A. & Oliveri, D. 1996 Wind- and rain-induced oscillations of cables of stayed bridges. *J. Wind Engng Indust. Aerodyn.* **64**, 171–185.

Bursnall, A. R. & Loftin, L. K. 1951 Experimental investigation of the pressure distribution about a yawed circular cylinder in the critical Remolds number range. NACA TN 2643.

Burton, D., Coa, D. Q., Tucker, R. W. & Wang, C. 2005 On the stability of stay cables under light wind and rain conditions. *J. Sound Vib.* **279**, 89–117.

Cantwell, B. J. & Coles, D. 1983 An experimental study of entrainment and transport in the turbulent near-wake of a circular cylinder. *J. Fluid Mech.* **136**, 321–374.

Cao, D. Q., Tucker, R. W. & Wang, C. 2003 A stochastic approach to cable dynamics with moving rivulets. *J. Sound Vib.* **268**, 291–304.

Carberry, J., Sheridan, J. & Rockwell, D. 2001 Forces and wake modes of an oscillating cylinder. *J. Fluids Struct.* **15**, 523–532.

Cheng, S. & Tanaka, H. 2005 Correlation of aerodynamic forces on an inclined circular cylinder. *Intl J. Wind Struct.* **8**(2), 135–146.

Cosentino, N., Flamand, O. & Ceccoli, C. 2003*a* Rain–wind induced vibration of inclined stay cables, Part I: Experimental investigation and physical explanation. *Intl J. Wind Struct.* **6**(6), 471–484.

Cosentino, N., Flamand, O. & Ceccoli, C. 2003*b* Rain–wind induced vibration of inclined stay cables, Part II: Mechanical modeling and parameter characterization. *Intl J. Wind Struct.* **6**(6), 485–498.

Davis, M. E. 1976 A comparison of the wake structure of a stationary and oscillating bluff body using conditional averaging technique. *J. Fluid Mech.* **75**, 209–231.

Fage, A. & Warsap, J. H. 1929 The effects of turbulence and surface roughness on the drag of a circular cylinder. *Aero. Res. Counc. Reports & Memo.* 1283, 1–14.

Farrel, C. & Blessmann, J. 1983 On critical flow around smooth circular cylinders. *J. Fluid Mech.* **136**, 375–391.

Flamand, O. 1995 Rain–wind induced vibration of cables. *J. Wind Engng Indust. Aerodyn.* **57**, 353–362.

Fox, T. A. & Apelt, C. J. 1993 Fluid-induced loading of a cantilevered circular cylinders in a low turbulence uniform flow. Part 3: fluctuating loads with aspect ratios 4 to 25. *J. Fluids Struct.* **7**, 375–386.

Gerrard, J. H. 1961 An experimental investigation of the oscillating lift and drag of a circular cylinder shedding turbulent vortices. *J. Fluid Mech.* **11**, 244–256.

Gerrard, J. H. 1966 The mechanics of the formation region of vortices behind bluff bodies. *J. Fluid Mech.* **25**, 401–413.

Goldstein, S. 1965 *Modern Development in Fluid Mechanics*. Dover.

Govardhan, R. & Williamson, C. H. K. 2000 Modes of vortex formation and frequency response of a freely-vibrating cylinder. *J. Fluid Mech.* **420**, 85–130.

Govardhan, R. & Williamson, C. H. K. 2001 Mean and fluctuating velocity fields in the wake of a freely-vibrating cylinder. *J. Fluids Struct.* **15**, 489–501.

Griffin, O. M. 1971 The unstready wake of an oscillating cylinder at low Reynolds number. *J. Appl. Mech.* **38**, 523–532.

Griffin, O. M. & Ramberg, S. E. 1974 The vortex street wakes of a vibrating cylinders. *J. Fluid Mech.* **66**, 729–738.

Griffin, O. M. & Votaw, C. W. 1972 The vortex street in the wake of a vibrating cylinder. *J. Fluid Mech.* **55**, 31–48.

Gu, M. & Du, X. 2005 Experimental investigation of rain–wind-induced vibration of cables in cable-stayed bridges and its mitigation. *J. Wind Engng Indust. Aerodyn.* **93**, 79–95.

Gu, M. & Lu, Q. 2001 Theoretical analysis of wind–rain induced vibration of cables of cable stayed bridges. *Proc. Fifth Asia Pacific Conf. on Wind Engng* pp. 125–128.

Gu, W., Chyu, C. & Rockwell, D. 1994 Timing of vortex formation from an oscillating cylinder. *Phys. Fluids* **6**(11), 3677–3682.

Guilmineau, E. & Queutey, P. 2004 Numerical simulation of vortex-induced vibration of a circular cylinder with low mass-damping in a turbulent flow. *J. Fluids Struct.* **19**, 449–466.

Hayashi, T. & Kawamura, T. 1995 Non-uniformity in a flow around a yawed circular cylinder. *Flow Meas. Instrumen.* **6**(1), 33–39.

Higuchi, H., Kim, H. J. & Farell, C. 1989 On flow separation and reattachment around a circular cylinder at critical Reynolds numbers. *J. Fluid Mech.* **200**, 149–171.

Hikami, Y. & Shiraishi, N. 1988 Rain–wind induced vibration of cables in cable stayed bridges. *J. Wind Engng Indust. Aerodyn.* **29**, 409–418.

Hover, F. S., Techet, A. H. & Triantafyllou, M. S. 1998 Forces on oscillating uniform and tapered cylinders in crossflow. *J. Fluid Mech.* **363**, 97–114.

Hover, F. S., Tvedt, H. & Triantafyllou, M. S. 2001 Vortex-induced vibrations of a cylinder with tripping wires. *J. Fluid Mech.* **448**, 175–195.

Hu, J. C., Zhou, Y. & Dalton, C. 2006 Effects of the corner radius on the near wake of a square prism. *Exps. Fluids* **40**, 106–118.

Huang, J. F., Zhou, Y. & Zhou, T. M. 2006 Three-dimensional wake structure measurement using a modified PIV technique. *Exps. Fluids* **40**, 884–896.

Igarashi, T. 1986 Effect of tripping wires on the flow around a circular cylinder normal to an airstream. *Bull. JSME* **29**(255), 2917–2924.

Kareem, A. & Cheng, C. M. 1999 Pressure and force fluctuations on isolated roughened circular cylinders of finite height in boundary layer flow. *J. Fluids Struct.* **13**, 907–933.

Keefe, R. T. 1962 Investigation of the fluctuating forces on a stationary circular cylinder in a subsonic stream and of the associated sound field. *J. Acoust. Soc. Am.* **34**, 1711–1714.

Khalak, A. & Williamson, C. H. K. 1996 Dynamics of a hydroelastic cylinder with very very low mass and damping. *J. Fluids Struct.* **10**, 455–472.

King, R. 1977 A review of vortex shedding research and its application. *Ocean Engng* **4**, 141–171.

Kiya, M. & Matsumura, M. 1988 Incoherent turbulence structure in the near wake of a normal plate. *J. Fluid Mech.* **190**, 343–356.

Krishnamoorthy, S., Price, S. J. & Paidoussis, M. P. 2001 Cross-flow past an oscillating circular cylinder: synchronization phenomena in the near wake. *J. Fluids Struct.* **15**, 955–980.

Laneville, A., Gartshore, I. S. & Parkinson, G. V. 1975 An explanation of some effects of turbulence on bluff bodies. *Proc. Fourth Intl Conf. Wind Effects on Buildings and Structures Heathrow, England*, K75–363, 333–341.

Leehey, P. & Hanson, C. E. 1971 Aeolian tones associated with resonant vibration. *J. Sound Vib.* **13**(4), 465–483.

Lemaitre, C. 2006 Dynamics of a rainwater film on a stay cable subject to wind. PhD thesis, Ecole Polytechnique, France.

Lemaitre, C., Alam, M. M., Hemon, P., Langre, E. & Zhou, Y. 2006 Rainwater rivulets on a cable subject to wind. *C. R. Méc.* **334**, 158–163.

Lesage, F. & Gartshore, I. S. 1987 A method of reducing drag and fluctuating side force on bluff bodies. *J. Wind Engng Indust. Aerodyn.* **25**, 229–245.

Matsumoto, M., Saitoh, T., Kitazawa, M., Shiraito, H. & Nishizaki, T. 1995 Response characteristics of rain–wind induced vibration of stay-cables of cable-stayed bridges. *J. Wind Engng Indust. Aerodyn.* **57**, 323–333.

Matsumoto, M., Yagi, T., Shigemura, Y. & Tsushima, D. 2001 Rain–wind induced vibration of inclined cables at limited high reduced wind velocity region. *Proc. Fifth Asia-Pacific Conference on Wind Engineering, Kyoto*, pp. 101–104.

Matsumoto, M., Yagi, T., Oishi, T. & Liu, Q. 2005*a* Motion-effect of water rivulet on rain–wind induced vibration of inclined cable. *Proc. Sixth Intl Symp. on Cable Dynamics (CD-R), September 19–22, Charleston, SC, USA.*

Matsumoto, M., Yagi, T., Sakai, S., Ohya, J. & Okada, T. 2005*b* Steady wind force coefficients of inclined stay cables with water rivulet and their application to aerodynamics. *Intl J. Wind Struc.* **8**(2), 107–120.

Matsumura, M. & Antonia, R. A. 1995 A laser-Doppler velocimetry study of ensemble-averaged characteristics of turbulent near wake of a square cylinder. *J. Fluid Mech.* **304**, 285–319.

Mei, V. C. & Currie, I. G. 1969 Flow separation on a vibrating circular cylinder. *Phys. Fluids* **12**, 2248–2254.

Mignolet, M. P. & Red-Horse, J. R. 1994 ARMAX identification of vibrating structures: model and model order estimation. *Proc. The 35th Structure and Structural Dynamics, and Material Conf. AIAA/ASME, Hilton Head, South Carolina, 18–20 April*, pp. 1628–1637.

Naumann, A. & Quadflieg 1972 Vortex generation on a cylindrical building and its simulation in wind tunnel. In *Proc. Flow Induced Structural Vibrations* IUTAM/IAHR *Symp.* (ed. E. Naudascher), pp. 730–747. Springer.

Nebres, J. & Batill, S. 1993 Flow about a circular with a single large-scale surface perturbation. *Exps. Fluids* **15**, 369–379.

Norberg, C. 2001 Flow around a circular cylinder: aspects of fluctuating lift. *J. Fluids Struct.* **15**, 459–469.

Norberg, C. 2003 Fluctuating lift on a circular cylinder: review and new measurements. *J. Fluids Struct.* **17**, 57–96.

Ohshima, K. 1987 Aerodynamic stability of the cables of a cable-stayed bridge subject to rain (a case study of the Ajigawa bridge). In *Proc. US–Japan Joint Seminar on Natural Resources*, pp. 324–336.

Okamoto, S., Uematsu, R. & Taguwa, Y. 2002 Fluid forces acting on two-dimensional circular cylinder in lock-in phenomenon. *JSME Int. J.* **45**, 850–856.

Oron, A., Davis, S. H. & Bankoff, S. G. 1997 Long-scale evolution of thin liquid films. *Rev. Mod. Phys.* **69**, 931–980.

Paranthoen, P., Browne, L. W. B., Masson, S. L., Dumouchel, F. & Lecordier, J. C. 1999 Characteristics of the near wake of a cylinder at low Reynolds numbers. *Eur. J. Mech.* B/*Fluids* **18**, 659–674.

Protos, A., Goldschmidt, V. W. & Toebes, G. H. 1968 Hydroelastic forces on bluff cylinders. In *Symp. on Unsteady Flow, Philadelphia, ASME*, 1–9.

Ramberg, S. E. 1983 The effects of yaw and finite length upon the vortex wakes of stationary and vibrating circular cylinders. *J. Fluid Mech.* **128**, 81–107.

Reisfeld, B. & Bankoff, S. G. 1992 Non-isothermal flow of a liquid film on a horizontal cylinder. *J. Fluid Mech.* **236**, 167–196.

Roshko, A. 1952 On the development of turbulent wakes from vortex street. PhD thesis, California Institute of Technology.

Roshko, A. 1954 On the drag and shedding frequency of two-dimensional bluff bodies. *NACA TN* 3169.

Ruscheweyh, H. & Verwiebe, C. 1995 Rain–wind-induced vibrations of steel bars. *Proc. Intl Symp. on Cable Dynamics, Liege, Belgium, 19–21 October*, pp. 469–472.

Sangil, K. & Sakamoto, H. 2006*a* Characteristics of fluctuating lift forces of a circular cylinder during generation of vortex excitation. *Wind Struc.* **9**, 109–124.

Sangil, K. & Sakamoto, H. 2006*b* Characteristics and suppression of flow-induced vibrations of two circular cylinders in tandem arrangement (1st Report). *Trans. JSME* B **72**, 314–321.

Sarpkaya, T. 1979 Vortex-induced oscillation – a selective review. *J. Appl. Mech.* **46**, 241–258.

Schewe, G. 1983 On the force fluctuations acting on a circular cylinder in cross-flow from subcritical up to transcritical Reynolds numbers. *J. Fluid Mech.* **133**, 265–285.

Son, J. S. & Hanratty, T. J. 1969 Velocity gradient at the wall for flow around a cylinder at Reynolds number from 5×10^3 to 10^5. *J. Fluid Mech.* **35**, 353–368.

Sung, J. & Yoo, J. Y. 2003 Near-wake vortex motions behind a circular cylinder at low Reynolds number. *J. Fluids Struct.* **17**, 261–274.

SURRY, D. 1972 Some effects of intense turbulent on the aerodynamic of a circular cylinder at subcritical Reynolds number. *J. Fluid Mech.* **52**, 543–563.

SZEPESSY, S. & BEARMAN, P. W. 1992 Aspect ratio and end plate effects on vortex shedding from a circular cylinder. *J. Fluid Mech.* **234**, 191–217.

TANEDA, S. & HONJI, H. 1967 Determination of the drag on vibrating circular cylinders. *Rep. Res. Inst. Appl. Mech.* **15**(50), 83–92.

TANIDA, Y., OKAJIMA, A. & WATANABE, Y. 1973 Stability of a circular cylinder oscillating in uniform flow or in a wake. *J. Fluid Mech.* **61**, 769–784.

THOMPSON, N. 1980 Mean forces, pressure and flow field velocities for circular cylindrical structures: single cylinder with two-dimensional flow. *EDU Data Item* 80025, London.

TING, D. S. K., WANG, D. J., PRICE, S. J. & PAIDOUSSIS, M. P. 1998 An experimental study on the fluidelastic forces for two staggered circular cylinders in cross-flow. *J. Fluids Struct.* **12**, 259–294.

TOEBES, G. H. 1969 The unsteady flow and wake near an oscillating cylinder. *Trans. ASME* D: *J. Basic Engng* **91**, 493–505.

VAN ATTA, C. W. 1968 Experiments on vortex shedding from yawed cylinders. *AIAA J.* **6**, 931–937.

VERWIEBE, C. & RUSCHEWEYH, H. 1998 Recent research results concerning the exciting mechanisms of rain–wind-induced vibrations. *J. Wind Engng Indust. Aerodyn.* **74–76**, 1005–1013.

WANG, Z. J., ZHOU, Y., HUANG, J. F. & XU, Y. L. 2005 Fluid dynamics around an inclined cylinder with running water rivulets. *J. Fluids Struct.* **21**, 49–64.

WEST, G. S. & APELT, C. J. 1982 The effect of tunnel blockage and aspect ratio on mean flow past a circular cylinder with Reynolds Number between 10^4 to 10^5. *J. Fluid Mech.* **14**, 361–377.

WEST, G. S. & APELT, C. J. 1997 Fluctuating lift and drag forces on finite lengths of a circular cylinder in the subcritical Reynolds number range. *J. Fluids Struct.* **11**, 135–158.

WILDE, K. & WITKOWSKI, W. 2003 Simple model of rain–wind-induced vibrations of stayed cables. *J. Wind Engng Indust. Aerodyn.* **91**, 873–891.

XU, S. J., ZHOU, Y. & WANG, M. H. 2006 A symmetric binary vortex street behind a longitudinally oscillating cylinder. *J. Fluid Mech.* **556**, 27–43.

XU, Y. L. & WANG, L. Y. 2003 Analytical study of wind–rain-induced cable vibration: SDOF model. *J. Wind Engng Indust. Aerodyn.* **91**, 27–40.

YAMAGUCHI, H. 1990 Analytical study on growth mechanism of rain vibration of cables. *J. Wind Engng Indust. Aerodyn.* **33**, 73–80.

YOSHIMURA, T., TANAKA, T., SASAKI, N., NAKATANI, S. & HIGA, S. 1988 Rain–wind induced vibration of the cables of the Aratsu Bridge. In *Proc. 10th National Conf. Wind Engineering, Tokyo*, pp. 127–132.

ZASSO, A., BOCCIOLONE, M. & BROWNJOHN, J. 1992 Rain–wind aeroelastic instability of the inclined hangers of a suspension bridge. *Proc. Inaugural Conf. of the Wind Engineering Society, Cambridge, September.*

ZDRAVKOVICH, M. M. 1997 *Flow Around Circular Cylinders. Vol. 1: Fundamentals*, Oxford Science.

ZDRAVKOVICH, M. M. 1982 Modification of vortex shedding in the synchronizing range. *Trans. ASME* I: *J. Fluids Engng* **104**, 513–517.

ZHANG, H. J., ZHOU, Y., SO, R. M. C., MIGNOLET, M. P. & WANG, Z. J. 2003 A note on the fluid damping of an elastic cylinder in a cross-flow. *J. Fluids Struct.* **17**, 479–483.

ZHANG, M. M., CHENG, L. & ZHOU, Y. 2004 Closed-loop-controlled vortex shedding from a flexibly supported square cylinder under different schemes. *Phys. Fluids* **16**, 1439–1448.

ZHOU, Y. & YIU, M. W. 2006 Flow structure, momentum and heat transport in a two-tandem-cylinder wake. *J. Fluid Mech.* **548**, 17–48.

ZHOU, Y., WANG, Z. J., SO, R. M. C., XU, S. J. & JIN, W. 2001 Free vibrations of two side-by-side cylinders in a cross-flow. *J. Fluid Mech.* **443**, 197–229.

ZHOU, Y., ZHANG, H. J. & YIU, M. W. 2002 The turbulent wake of two side-by-side circular cylinders. *J. Fluid Mech.* **458**, 303–332.